NUMERICAL MODELING OF HETEROGENEITY WITHIN A FLUVIAL POINT-BAR DEPOSIT USING OUTCROP AND LIDAR DATA: WILLIAMS FORK FORMATION, PICEANCE BASIN, COLORADO

by

AMANDA IRENE ELLISON

B.S., Colorado State University, 2002

A thesis submitted to the

Faculty of the Graduate School of the

University of Colorado in partial fulfillment

of the requirement for the degree of

Master of Science

Department of Geological Sciences

2004

This thesis entitled:

Numerical Modeling of Heterogeneity Within

a Fluvial Point-Bar Deposit Using Outcrop and Lidar Data:

Williams Fork Formation, Piceance Basin, Colorado

written by Amanda Irene Ellison

has been approved for the Department of Geological Sciences

Matthew J. Pranter

Rex D. Cole

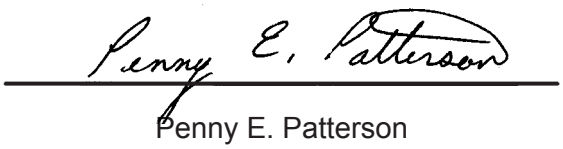

Penny E. Patterson

Date July 26, 2004

The final copy of this thesis has been examined by the signatories, and we find that both the content and the form meet acceptable standards of scholarly work in the above mentioned discipline.

ABSTRACT

Ellison, Amanda Irene (M.S., Geology [Department of Geological Sciences])

Numerical Modeling of Heterogeneity Within a Fluvial Point-Bar Deposit Using Outcrop and Lidar Data: Williams Fork Formation, Piceance Basin, Colorado

Thesis directed by Assistant Professor Matthew J. Pranter

This study utilizes detailed outcrop measurements, high-resolution lidar data, and numerical modeling to investigate the effects of stratigraphic and petrophysical heterogeneity on fluid flow and storage within fluvial point-bar deposits. Results suggest that the internal heterogeneities present within point-bar deposits can have an impact on fluid flow on a production time scale and hence, should be included in reservoir modeling.

Outcrops of a point bar within the Lower Williams Fork Formation located in Coal Canyon, western Colorado were used to generate two-dimensional (2-D) and three-dimensional (3-D) geologic models. These models represent different lithologic and petrophysical distributions, based on detailed sedimentologic and stratigraphic analyses of the outcrop, and were compared to determine their impact on fluid flow and storage. Results show that lithologic heterogeneity has a significant affect on fluid flow, while petrophysical heterogeneity is more significant when evaluating fluid storage.

Lithologic discontinuities compartmentalize the reservoir and act as baffles to fluid flow. The effect of these heterogeneities is contingent on the orientation of the point bar with respect to fluid flow. Perpendicular to paleoflow, lithologic discontinuities act as flow baffles, and lead to relatively higher breakthrough times

and lower sweep efficiency. Parallel to paleoflow, shale drapes focus the flow and result in lower breakthrough time and higher sweep efficiency.

The method used to distribute petrophysical properties has a significant affect on estimated pore volume in a reservoir. The distributions of porosity and permeability based on grain-size trends in outcrop cause fluid to be focused at the base of the reservoir, negatively affecting breakthrough time and sweep efficiency.

DEDICATION

I would like to dedicate this thesis first and foremost to my parents who have always believed in me and have shaped me into the person I am today. I could not have accomplished any of this without your love and support.

And to Jason, for always being there for me and reminding me of what is really important in life. You have been the most solid and dependable rock in this geologist's world. We are now one step closer to being together.

ACKNOWLEDGEMENTS

I would first of all like to thank my advisor Dr. Matthew Pranter for his guidance and patience throughout this entire process. You have given me the knowledge and confidence that I know will help me succeed in the future. I would like to express my thanks to Dr. Rex Cole, who first introduced me to these spectacular outcrops and for his guidance in the field and throughout this project. And I would also like to thank Dr. Penny Patterson for helping to bring this project together and for her suggestions regarding field work and modeling.

This research was funded by the Department of Geological Sciences through a teaching assistantship and a research assistantship through the Reservoir Characterization and Modeling Laboratory (RCML). Grants were received from the American Association of Petroleum Geologists (AAPG) Grants-In-Aid Program (Nancy Setzer Murray Memorial Grant), the Rocky Mountain Association of Geologists (RMAG) Norman H. Foster Memorial Grant, and the International Association of Mathematical Geologists (IAMG) Student Grant Program.

Funding for lidar acquisition and processing was provided by ExxonMobil Upstream Research Company. Dave Jennette and Florence Bonnaffe of the Texas Bureau of Economic Geology (BEG) provided valuable assistance with lidar processing and interpretation. Neil Hurley provided the gamma ray scintillometer used in the field. Neil Hurley, Mike Gardner, Steve Cumella, and Mary Kraus offered useful suggestions and assistance with various aspects of this research.

I would like to thank my field assistants, Tim Smith and Quentin German for braving the heat, mosquitoes, and heights that come along with field work. Also thanks to Quentin German, Colette Hirstius, Marielis Vargas, Lauri Burke and Stephanie Gaswirth for their valuable advice and friendship throughout this process.

CONTENTS

CHAPTER **PAGE**

ABSTRACT..... iii

DEDICATION..... v

ACKNOWLEDGEMENTS.....vi

CONTENTS..... vii

LIST OF TABLES.....x

LIST OF FIGURES.....xi

I. INTRODUCTION..... 1

OBJECTIVES..... 1

STUDY AREA..... 2

GEOLOGIC SETTING..... 6

Regional Structure.....6

Stratigraphy.....9

Late Cretaceous Paleogeography.....13

Petroleum Geology..... 13

II. SEDIMENTOLOGY AND STRATIGRAPHY.....18

INTRODUCTION..... 18

SEDIMENTOLOGY..... 18

Methods..... 18

Facies Descriptions.....23

Facies Interpretation and Analysis..... 29

Facies Association..... 34

STRATIGRAPHIC ARCHITECTURE..... 36

Methods..... 36

Architectural Analysis.....37

DEPOSITIONAL SETTING.....40

PALEOCHANNEL RECONSTRUCTION.....44

Paleohydraulic Interpretation.....44

Paleochannel Morphology.....45

Discussion..... 52

III. TWO-DIMENSIONAL OUTCROP MODELING..... 54

MODELING OBJECTIVES..... 54

MODELING FRAMEWORK..... 55
Lidar Data..... 55
Lidar Acquisition, Processing, and Interpretation.....56
Grid Construction.....61
LITHOLOGY MODELING.....64
Methods.....64
Results.....65
Discussion.....65
GRAIN-SIZE MODELING.....68
Methods.....68
Results.....68
Discussion.....70
PETROPHYSICAL MODELING.....70
Modeling Scenarios.....70
Porosity Modeling.....71
Permeability Modeling.....85
VOLUMETRICS.....94
Methods.....94
Results.....95
Discussion.....101
STREAMLINE SIMULATION.....102
Methods.....102
Results.....103
Discussion.....113
IV. THREE-DIMENSIONAL POINT-BAR MODELING..... 116
MODELING OBJECTIVES.....116
MODELING FRAMEWORK..... 117
Point-Bar Geometry.....117
Grid Construction.....119
LITHOLOGY MODELING.....119
Methods.....119
Results.....121
Discussion.....121
GRAIN-SIZE MODELING..... 124

Methods……124
Results……125
Discussion……125
PETROPHYSICAL MODELING……127
Modeling Scenarios……127
Porosity Modeling……127
Permeability Modeling……136
VOLUMETRICS……145
Methods……145
Results……145
Discussion……147
STREAMLINE SIMULATION……149
Methods……149
Results……150
Discussion……164
V. CONCLUSIONS AND RECOMMENDATIONS……167
CONCLUSIONS……167
Sedimentology and Stratigraphy……167
2-D Outcrop Modeling……168
3-D Point-Bar Modeling……169
2-D and 3-D Modeling Comparison……170
RECOMMENDATIONS……171

REFERENCES……173

APPENDIX

A. MEASURED SECTION DATA……182
B. 2-D OUTCROP MODELS……199
C. LIDAR DATA……201
D. 2-D PETROPHYSICAL MODEL STATISTICS……203
E. ANALYSIS OF VARIANCE FOR 2-D MODELS……206
F. 3-D POINT-BAR MODELS……220
G. 3-D PETROPHYSICAL MODEL STATISTICS……222
H. ANALYSIS OF VARIANCE FOR 3-D MODELS……225

LIST OF TABLES

2.1: Summary of Fluvial Facies……31

2.2: Paleochannel Morphology Equations and Results……47

3.1: Lithology Model Descriptions……66

3.2: Methods of Petrophysical Property Distribution……..72

3.3: Model Labeling Scheme……73

3.4: Summary of Drainable Volumes……99

3.5: Pore-Volume Calculation Results……...100

3.6: Streamline Simulation Parameters……104

3.7: Summary of Streamline Simulation Results……..105

4.1: Bulk-Sand Volume Results……..146

4.2: Pore-Volume Calculation Results……...148

4.3: Summary of Streamline Simulation Results, Well Pattern 1……...151

4.4: Summary of Streamline Simulation Results, Well Pattern 2……...152

4.5: Comparison of Streamline Simulation Results, Well Patterns 1 and 2….166

LIST OF FIGURES

1.1: Piceance Basin Location Map……. 3

1.2: Digital Elevation Map of Coal Canyon……4

1.3: Coal Canyon Topographic Map……...5

1.4: Outcrop Study Area Topographic Map……...7

1.5: Piceance Basin Geologic Map……8

1.6: Piceance Basin Regional Cross Section……. 10

1.7: Piceance Basin Stratigraphic Column……..11

1.8: Extent of Western Interior Seaway……... 14

1.9: Regional Late Cretaceous Paleogeography……15

1.10: Depositional Setting of Lower Williams Fork Formation……. 16

2.1: Measured Section Locations (West Side)……20

2.2: Measured Section Locations (East Side)……21

2.3: Ascending a Measured Section……22

2.4: Fluvial Facies……24

2.5: Trough Cross Beds……. 25

2.6: Teredolites Burrows…… 26

2.7: Climbing Ripples……..28

2.8: Basal Scour Surface……30

2.9: Idealized Measured Section……...35

2.10: Architectural Analysis of NW Outcrop……38

2.11: Fluvial Depositional Settings……41

2.12: Outcrop Paleocurrent Data……..42

2.13: Bedform Phase Diagram……..46

2.14: Schematic Meander Bend……49

3.1: Optech Ilris 3-D Laser Scanner……57

3.2: Lidar Scans……...58

3.3: Lidar Workflow…… 59

3.4: Lidar VRML Model……...60

3.5: Interpreted Lidar Point-Cloud……62

3.6: Outcrop Model Framework……63

3.7: Outcrop Lithology Models……...67

3.8: Outcrop Grain-Size Model……..69

3.9: Model Variograms……75

3.10: Grain Size to Porosity Transform……77

3.11: Porosity Model Distributions…… 78

3.12: Uniform Porosity Models……..79

3.13: Conditionally Simulated Porosity Models…….. 81

3.14: Conditionally Simulated Porosity Models with Trend…….. 82

3.15: Grain-Size Porosity Model……...83

3.16: Porosity to Permeability Transform…… 87

3.17: Permeability Distribution Models……88

3.18: Uniform Permeability Models…….. 89

3.19: Conditionally Simulated Permeability Models……...91

3.20: Conditionally Simulated Permeability Models with Trend……...92

3.21: Grain-Size Permeability Models……..93

3.22: Drainable Volume Lithology Model 1…… 96

3.23: Drainable Volume Lithology Model 2…… 97

3.24: Drainable Volume Lithology Model 3…… 98

3.25: BTT Comparison…… 106

3.26: TFI at BTT for Uniform Models……..107

3.27: TFI at BTT for Conditionally Simulated Models……..108

3.28: TFI at BTT for Conditionally Simulated Models with Trend……..109

3.29: TFI at BTT for Grain-Size Models……110

3.30: Volume Swept Comparison……...112

4.1: Lidar and Point-Bar Model……...118

4.2: 3-D Model Framework……..120

4.3: Lithology Models Perpendicular to Paleoflow……...122

4.4: Lithology Models Parallel to Paleoflow……...123

4.5: Grain-Size Model……...126

4.6: Porosity Models Summary……...129

4.7: Uniform Porosity Models Perpendicular to Paleoflow……. 130

4.8: Uniform Porosity Models Parallel to Paleoflow……131

4.9: CS Porosity Models Perpendicular to Paleoflow……..132

4.10: CS Porosity Models Parallel to Paleoflow……...133

4.11: Grain-Size Porosity Model……135

4.12: Permeability Models Summary……137

4.13: Uniform Permeability Models Perpendicular to Paleoflow……138

4.14: Uniform Permeability Models Parallel to Paleoflow……...139

4.15: CS Permeability Models Perpendicular to Paleoflow…… 140

4.16: CS Permeability Models Parallel to Paleoflow……141

4.17: Grain-Size Permeability Models Perpendicular to Paleoflow……...143

4.18: Grain-Size Permeability Models Parallel to Paleoflow……...144

4.19: TFI at BTT for Uniform Models with Well Pattern 1……153

4.20: TFI at BTT for Uniform Models with Well Pattern 2……...154

4.21: TFI at BTT for CS Models with Well Pattern 1……155

4.22: TFI at BTT for CS Models with Well Pattern 2……156

4.23: TFI at BTT for Grain-Size Models with Well Pattern 1……..157

4.24: TFI at BTT for Grain-Size Models with Well Pattern 2……...158

4.25: BTT Comparison for Well Pattern 1……. 159

4.26: BTT Comparison for Well Pattern 2……. 160

4.27: Volume Swept Comparison for Well Pattern 1……...162

4.28: Volume Swept Comparison for Well Pattern 2……...163

CHAPTER ONE

INTRODUCTION

OBJECTIVES

Characterization and modeling of fluvial reservoirs are often challenging for geologists due to the 3-D complexity of fluvial deposits and their various scales of heterogeneity (Jackson, 1977; Miall, 1988; Willis, 1989; Sharp et al., 2003). For example, the analysis of field-scale heterogeneities is mainly concerned with the distribution and connectivity of reservoir sand bodies. Yet, there are additional levels of heterogeneity at the intra-field scale that also affect reservoir prediction and performance. The stratigraphic architecture of fluvial deposits is difficult to incorporate in traditional reservoir models due to the relatively limited lateral extent of elements and bounding surfaces, which is often less than the typical well spacing in developed fields (Miall, 1988). In the case of a point-bar reservoir, the most common internal architectural features are lateral-accretion surfaces. These depositional surfaces (time lines) can influence reservoir behavior (Swanson, 1993). These surfaces are potential baffles and barriers to flow that are typically unaccounted for in traditional reservoir models. Internal facies variations, such as the vertical change from trough cross-bedded to ripple-laminated sandstone, produce a fining-upward trend in grain size and corresponding decrease in porosity and permeability. The distribution of lithologies and petrophysical properties within a reservoir model has a significant impact on the prediction of fluid flow and storage.

The goals of this study were to address the following questions: (1) how do facies trends and architecture vary spatially within a point-bar deposit?; (2) how do lithologic heterogeneities (e.g. shale-draped lateral-accretion surfaces) affect fluid

flow and storage within a point-bar deposit?; and (3) how does the distribution of petrophysical properties within a point bar affect fluid flow and storage?

These questions are addressed by constructing detailed outcrop models of a well-exposed point-bar sandstone in the Williams Fork Formation (Campanian), Colorado. This outcrop is ideally suited for constructing lithology and grain-size models to test various levels of internal heterogeneity. Using the lithology models as constraints, four methods of distributing petrophysical properties were employed to test the relative affect of these heterogeneities on fluid flow and storage. Although fluvial reservoirs are diverse and unique, there is a set of criteria that links them, including the geometry and origin of the depositional system and the geometry of the reservoir body (Schumm, 1963; Miall, 1996). Therefore, the results of this study are applicable to point-bar reservoirs around the world. This includes those found in both meandering and braided fluvial systems, assuming that appropriate scaling factors are considered.

STUDY AREA

The Piceance Basin is located in western Colorado and covers an area of 18,700 km^2 (7,225 mi^2) (Figure 1.1). This asymmetric foreland basin trends northwest-southeast and is approximately 160 km (100 mi) long and 64 to 80 km (40 to 50 mi) wide (Spencer, 1989).

On the western margin of the basin, the Little Book Cliffs provide excellent outcrop exposures of the Upper Cretaceous section within a series of canyons. Coal Canyon, which is located near the town of Palisade, Colorado, is approximately 300 m (1,000 ft) deep and extends for 6.4 km (4 mi). The canyon walls provide outcrop views of both depositional strike and depositional dip for the Williams Fork Formation (Figure 1.2 and 1.3). This canyon is located within the Little Book Cliffs Wild Horse

Refuge, which extends over an area of 122 km^2 (47 mi^2) at elevations from 1,500 to 2,200 m (5,000 to 7,300 ft). Access to the field area is along Coal Canyon road, a well-used four-wheel-drive road. During the months of December through May, access by vehicle is restricted by a gate maintained by the Bureau of Land Management (BLM). The focus of this study is a point-bar sand body that can be viewed in a series of three outcrops that occur along Coal Canyon Road within several hundred meters of each other. Herein, they are referred to as the northwest outcrop, southwest outcrop, and east outcrop, as defined below (Figure 1.4).

Overall transport direction of the fluvial point bar is to the east, hence, the northwest outcrop, which is oriented in a NNE-SSW direction and is approximately 200 m (656 ft) long and 9 m (30 ft) high, is oriented approximately perpendicular to the general paleoflow direction of fluvial systems and is the object of 2-D modeling. The east outcrop, which is oriented approximately E-W and extends 125 m (410 ft) long and 11 m (36 ft) high, provides a view approximately parallel to paleoflow. The southwest outcrop, oriented in a NE-SW direction, provides an oblique view relative to paleoflow. It extends 100 m (328 ft) and is approximately 8 m (26 ft) high.

GEOLOGIC SETTING

Regional Structure

The Piceance Basin is an intermountain basin that is located in northwestern Colorado. It is bounded by the Uinta Mountain Uplift on the northwest, the Axial Arch on the north, the White River Uplift on the east, the Elk Mountains and Sawatch Uplift on the southeast, the Gunnison Uplift and San Juan volcanic field on the south, the Uncompahgre Uplift on the southwest, and the Douglas Creek Arch on the west. The basin is a northwest-southeast trending elongate basin that dips gently on the western flank and is steeply dipping to overturned on the eastern flank (Figure 1.5

and 1.6; Tyler and McMurry, 1995). The structural complexity on the eastern margin of the basin, as seen in outcrops at the Grand Hogback, is the result of high-angle thrust faults (Cole et al., 2002).

The Piceance Basin is one of many intermountain basins that formed during the Laramide Orogeny, which began in the Campanian and continued through to the Eocene (Tweto, 1975). A major episode of deformation occurred during the early stages of the Laramide Orogeny, which is characterized by thrusting along the eastern margin of the basin. The Grand Hogback monocline is the result of a blind, basement-involved thrust wedge, which also created the Divide Creek and Wolf Creek anticlines (Perry et al., 1988). The thrust system is underlain by a decóllement that developed due to mechanically weak evaporites in the Middle Pennsylvanian section (Grout and Verbeek, 1992). Recent studies have suggested that wrench tectonics is the dominant structural style of the basin as determined by the identification of left-lateral, transpressional elements in 3-D seismic data (Cumella and Ostby, 2003).

Stratigraphy

The Lower Williams Fork Formation is a member of the Upper Cretaceous Mesaverde Group (Figure 1.7). Several naming conventions have been designated for the Cretaceous strata in the Piceance Basin. On the western margin, the Mount Garfield Formation and the Hunter Canyon Formation are exposed in the Little Book Cliffs area. Equivalent to those strata on the eastern margin of the basin are the Iles and Williams Fork Formations, which is also the naming convention used in the subsurface. Due to the widespread acceptance of the subsurface terminology, these names are used in this study.

The Mesaverde Group represents the final regressive period of the Western Cretaceous Interior Seaway. The sequence-stratigraphic framework of the Mesaverde Group has been defined by several authors using subsurface and outcrop data (Hettinger and Kirschbaum, 2002; Patterson et al., 2003). The basal portion of the Mesaverde Group consists of two composite sequences, the first of which includes the highstand deposits of the Castlegate Sandstone, Sego Sandstone, and the progradational Corcoran Member of the Iles Formation. The second composite sequence consists of the lowstand portion of the Corcoran and Cozzette members of the Iles Formation and the transgressive and highstand deposits of the Rollins Formation (Patterson et al., 2003). These members are divided by tongues of the Mancos Shale (Hettinger and Kirschbaum, 2002). The Williams Fork Formation and Ohio Creek Conglomerate represent five composite sequences. The Williams Fork Formation has an average thickness between 1,100 and 1,600 m (3,600 and 5,155 ft), thinning to the west to about 360 m (1,200 ft). This thinning has been attributed to erosional scour of the overlying intervals, including the Ohio Creek Conglomerate (Patterson et al., 2003) and the Wasatch Formation (Hettinger and Kirschbaum, 2002), along a regional unconformity. In addition, it has been attributed to variation in subsidence rate across the basin (Hettinger and Kirschbaum, 2002). In an alluvial environment, lowstand deposits are defined by the presence of thick, laterally extensive high net-to-gross intervals while the transgressive and highstand deposits tend to have more isolated channels and a lower net-to-gross (Patterson et al., 2003). The lower third of the Williams Fork is a low net-to-gross interval with approximately 30 to 60% sand while the upper portion has a net-to-gross between 50 to 80% (Cole and Cumella, 2003).

Late Cretaceous Paleogeography

Cretaceous rocks of western Colorado and eastern Utah were deposited in association with the transgressions and regressions of the Western Interior Seaway that extended from the Arctic down to the present-day Gulf of Mexico (Figure 1.8). Sediments from the Sevier Orogeny were being shed off of the highlands in western Utah and carried by fluvial systems to coastal areas forming coal wetlands (Figure 1.9; Hettinger and Kirschbaum, 2002). In general, the Cretaceous stratigraphic interval is represented as a progradational succession consisting of non-marine environments situated to the west and marine environments situated to the east that developed as a result of the final regression of the epiric seaway. Within the Piceance Basin, the non-marine environments include braid-plain (Upper Williams Fork), upper and lower coastal plain (Lower Williams Fork), marginal-marine (Iles), and marine (Mancos). The Lower Williams Fork, which is the interval of interest in this study, was deposited during the Campanian Stage of the Cretaceous Period in a coastal-plain environment with meandering streams, swamps, and floodplains (Figure 1.10) These deposits are characterized by isolated sandstones (e.g. point-bar sand bodies) encased in floodplain mudstones and coals.

Petroleum Geology

Upper Cretaceous rocks of the Piceance Basin form an unconventional petroleum system which is of economic importance in the western United States. It is considered a basin-centered gas system, characterized by regionally pervasive gas accumulations, abnormal reservoir pressures, and low permeabilities (Law, 2002). Recent estimates suggest that the Piceance Basin contains between 566 billion and 1.13 trillion m^3 (20 and 40 tcf) of recoverable gas (USGS, 2003; Potential Gas Committee, 2003). Production occurs mainly from fractured, low-matrix

permeability (0.1 to 2 μd) sandstones of the Lower Williams Fork Formation (Cumella and Ostby, 2003). This low permeability is the result of authigenic clays, carbonate cement, and quartz overgrowths which occurred over a period of intense regional diagenesis (Johnson, 1989; Kuuskraa et al., 1997). The Cameo coal interval, which occurs at the base of the Williams Fork Formation, and organic shales within the Mesaverde Group and Mancos Shale (i.e. Type II and III kerogen), are the source of the overlying gas (Tyler and McMurry, 1995). Timing of gas generation coincides with maximum burial of the reservoir interval during the Oligocene Epoch (33.7 to 23.8 Ma) (Payne et al., 2000). The dominant trapping mechanism is stratigraphic, related to the stacking of fluvial sand bodies surrounded by floodplain mudstones; although structural-stratigraphic traps are also present (Spencer, 1989).

CHAPTER TWO

SEDIMENTOLOGY AND STRATIGRAPHY

INTRODUCTION

Sedimentologic and stratigraphic interpretation of fluvial deposits in outcrop is an important step in developing subsurface analogs for use in reservoir characterization and geologic modeling. Specific studies include facies analysis, defining the stratigraphic architecture, interpretation of depositional setting, and paleohydraulic and paleomorphologic reconstruction. Detailed sedimentologic descriptions that include both qualitative and quantitative data are used to define and interpret lithofacies and facies associations. These descriptions are useful for populating lithology and grain-size models, as well as inferring spatial variation in petrophysical properties. Architectural analysis of the outcrops delineates a hierarchical stratigraphic framework that is utilized in building the modeling grid. The sedimentology and stratigraphy of the outcrops studied within Coal Canyon are merged to interpret the depositional environment of these deposits. This step is crucial in order to use the results of this study as an analog for subsurface cases. Reconstruction of the paleochannel morphology and flow conditions responsible for the deposition of the outcrop deposits is accomplished using empirically derived relationships. Morphologic parameters, such as meander wavelength and sinuosity, are useful for constructing the geometry and orientation of the fluvial deposits in 3-D.

SEDIMENTOLOGY

Methods

Detailed sedimentologic observations and measurements were collected from the three outcrops within Coal Canyon to describe the Williams Fork deposits. The

purpose of these descriptions is to provide adequate data to compute geostatistical parameters that characterize lithologic and grain-size distributions, their relative proportion within reservoir sand bodies, and their horizontal and vertical correlation lengths (Joseph et al., 2000). Thirteen stratigraphic sections were measured that include two on the southwest outcrop, five on the northwest outcrop, and six on the east outcrop (Figure 2.1 and 2.2). Field work was completed in two phases. The first phase was conducted in August 2003. Six measured sections were completed which required lateral traversing of the outcrop due to limited accessibility. Phase two was completed in March 2004 and seven vertical sections were acquired by ascending up section and rappelling down (Figure 2.3). The measured sections have an average length of 11 m (36 ft). Average lateral spacing between sections for each outcrop was 96 m (315 ft) for the southwest, 27 m (89 ft) for the northwest, and 24 m (79 ft) for the east outcrop, respectively. Sedimentologic descriptions were recorded on a centimeter-scale using a standard sedimentary log and include mineralogy, texture (e.g. grain size, grain shape, and grain sorting), bed thickness, bed contacts, and sedimentary structures including those of depositional, erosional, and biogenic origin. Twenty-six paleocurrent measurements were collected using a Brunton compass from both erosional (flute casts) and depositional (cross-beds) structures along the outcrop. A gamma-ray profile, measured in counts per second (cps), was collected along the six laterally-traversed measured sections using a GRS-500 Gamma Ray Spectrometer/Scintillometer (property of Neil Hurley, Colorado School of Mines). The scintillometer uses a sodium iodide crystal and a high-stability photomultiplier tube for detection and is calibrated using barium-133. Areas of missing data on the measured sections represent covered intervals.

Facies Descriptions

The Williams Fork strata described in outcrops of Coal Canyon comprise six main lithofacies types, which were identified on the basis of their characteristic lithology and sedimentary structures (Figure 2.4). These facies include trough cross-bedded sandstone, current-rippled sandstone, nodular siltstone, laminated siltstone, conglomeratic mud-chip sandstone, and coal and bentonite beds.

Facies A: trough cross-bedded sandstone

Trough cross-bedded sandstone is the most common facies type within the point-bar deposit (Figure 2.4 A). It consists of a light brown to rusty colored, trough cross-bedded lithic sandstone. The sandstone is composed of approximately 70% quartz and 30% lithic fragments. Grain size varies from fine to lower medium sand, with moderate sorting and rounding. Trough cross-bed height set thickness varies from 20 to 50 cm (7.9 to 19.7 in), and cross-bed width varies from 1 to 3 m (3.3 to 9.8 ft). Foresets are concave up with tangential lower contacts (Figure 2.5). Reactivation surfaces are common between and within cross-bed sets. Tabular cross beds are less common, but are still present within this facies. Minor structures that are often associated with this facies include soft-sediment deformation features (e.g. load structures, flute casts), animal burrows (e.g. *Teredolites*; Figure 2.6), and siderite nodules.

Facies B: current-rippled sandstone

Current-rippled sandstone facies is composed of light brown to rusty colored, ripple-laminated sandstone (Figure 2.4 B). Grain size varies from upper very fine to fine, with moderate sorting and rounding. The ripples are asymmetrical and preserved dominantly on the lee-side but are occasionally preserved on the stoss-

side. The average ripple height is approximately 0.4 cm (0.16 in), with an average ripple length of 4 cm (1.6 in), yielding a ripple index of 10. The ripple index is the ratio of ripple length to ripple height and is used to identify whether flow is uni- or multi-directional (Leeder, 1999). The ripples often occur in cosets up to 5 cm (in) thick with horizontal to low-angle boundaries, indicating ripple drift (i.e. climbing ripples; Figure 2.7). Thin mud drapes (< 2 mm) are occasionally present between ripple laminae sets. Other minor structures associated with this facies include horizontal laminations (cm-scale), siderite nodules, and animal burrows (e.g. *Arenicolites*).

Facies C: nodular siltstone

Nodular siltstone facies consists of a mottled, nodular, silt-dominated mudstone with intercalations of fine-grained sand (Figure 2.4 C). The nodules range in size from 5 to 30 cm (2 to 11.8 in) and are composed of silt-rich mudstone. Root traces, bioturbation, carbonaceous material and siderite concretions are common within this facies.

Facies D: laminated mudstone

Laminated mudstone facies is composed of light to dark gray, silt-dominated mudstone with moderate amounts of carbonaceous material (Figure 2.4 D). The mudstone exhibits laminations that are 1 to 2 mm (0.04 to 0.08 in) thick. The degree of bioturbation varies from moderate to high. Root traces and siderite concretions are also present in varying amounts.

Facies E: conglomeratic mud-chip sandstone

Conglomeratic mud-chip sandstone facies consists of poorly-sorted, conglomeratic sandstone with 75 to 85% matrix (Figure 2.4 E). The matrix is composed of lower medium to upper fine grained, moderately-sorted sandstone. Mud-chip clasts vary in size from 0.5 to 2 cm (0.2 to 0.8 in) and are sub-angular to moderately rounded. The most common occurrence of this facies is just above erosional and scoured surfaces, such as the base of the main sand body within the measured sections (Figure 2.8).

Facies F: coal and bentonite beds

Coal and bentonite beds range from 20 to 30 cm (7.9 to 11.8 in) thick (Figure 2.4 F). Two prominent coal beds, separated by a layer of bentonite are recognized at the base of all three outcrops that were described. Cole et al. (2002) suggests that the coals are bituminous in rank with abundant carbonaceous material. Coals within the Piceance Basin vary from high-volatile C to high-volatile B (Cole et al., 2002) Vertical cleats are common within the coal seams and have a spacing from 2 to 5 cm (0.8 to 2 in).

Facies Interpretation and Analysis

Detailed sedimentologic descriptions of facies are used to interpret the conditions under which the various facies formed. The results of the facies interpretation and analysis are summarized in Table 2.1.

Facies A: trough cross-bedded sandstone

The presence of both trough and tabular cross-beds in this facies indicate deposition by bedload traction under dominantly unidirectional currents. Spoon-

shaped scours form the bounding surfaces of trough cross sets. These may have formed by several mechanisms, including eddies at the advancing front of sand waves, migrating linguoid forms, or vortices moving in the direction of stream flow (Harms et al., 1962). The scours were subsequently filled by bedload sediment avalanching down the slip face of the dune. The size of the dunes is related to flow depth and largely independent of grain size (Allen, 1984). A ratio of 1:6 has been suggested for the relationship between dune height and flow depth, although it should only be used as a generalization due to the strong 3-D nature of dunes (Collinson and Thompson, 1989). Using this relationship and the height of dunes recorded in outcrop, the approximate flow depth may have been between 1.2 and 3 m (3.9 to 9.8 ft). Trough cross-bedding indicates that the depositing currents were flowing in primarily one direction. Trough cross-bedding has been observed in stream, near-shore marine, beach, and eolian deposits (Harms et al., 1962). Therefore, facies associations must be used to delineate the depositional environment. Reactivation surfaces are the result of bedforms re-scaling to the current conditions, and therefore indicate fluctuations in water depth (Middleton, 1965). The soft-sediment deformation occurred as a result liquefaction, caused by an increase in pore pressure. These structures were likely formed post-depositionally.

Facies B: Current-rippled sandstone

Ripple laminations are deposited by bedload traction processes, but at lower flow velocities than that of cross beds. Using the ripple index calculated from the ripple height and wavelength, wave versus current ripples can be distinguished. The ripple index for Facies B does not provide conclusive evidence, although most current ripples have indices between 10 and 40 (Leeder, 1999). The asymmetrical

shape of the ripple crest also indicates that these are current ripples. The strongly 3-D nature of the ripples indicates a highly sinuous crest line, such as linguoid ripples (Collinson and Thompson, 1989). Both Type A (erosional-stoss) and Type B (depositional-stoss) climbing ripples are present. Type A indicates low aggradation rates relative to ripple migration while Type B ripples are produced by high aggradation rates relative to ripple migration (Ashley et al., 1982). The mud drapes are the result of suspension fall-out during periods of little to no ripple migration.

Facies C and D: nodular and laminated siltstone

Mudstones are deposited mainly by vertical-accretion processes, such as suspension fallout. Change in lamination thickness or color indicates grain size changes and long-term fluctuations in sediment load (Collinson and Thompson, 1989). The nodular texture, mottled color, and rooting indicates alteration by pedogenic processes or shallow lake deposition.

Facies E: conglomeratic mud-chip sandstone

Conglomeratic mud-chip sandstone deposits formed during the incision or lateral erosion of a fluvial channel into previously existing floodplain deposits. The angularity of mud-chips infers that they may have been carried some distance before being deposited as poorly sorted, non-stratified beds. This deposit is known as a lag and was out of equilibrium with flow conditions during its generation (Allen, 1984).

Facies F: coal and bentonite beds

Coal beds are formed by the vertical accretion of plant material where there is little sediment influx. The continuity of the coal beds across the Coal Canyon study area indicates a period of infrequent channel activity. Bentonite beds are a result of

diagenesis of volcaniclastic ash, mainly the formation of smectitic clays from andesitic rocks (Nichols, 1999).

Facies Association

A vertical (or horizontal) sequence of facies is referred to as a facies association (Anderton, 1985). Walther's Law states that if two facies are adjacent to one another in a vertical sequence and they are not separated by surfaces of erosion, they were likely deposited in adjacent depositional environments (Anderton, 1985). The measured sections reveal a repeated succession of facies. An idealized measured section was generated by incorporating common features seen in all the measured sections (Figure 2.9; see Appendix A for all measured section data). The base of many of the measured sections is at the lower coal bed and separated from an upper coal bed by a layer of bentonite ash. The next facies present are the laminated and nodular siltstones. At several localities, these two facies have been eroded away and the next facies, trough cross-bedded sandstone, is in direct contact with the upper coal bed. The conglomeratic mud-chip sandstone is often found at the base of the sand body, along with the more dominant trough cross-bedded sandstone. Current-rippled sandstone is the next facies encountered within the section, and is overlain dominantly by laminated, and occasionally nodular, siltstone. The final facies present within the sequence is ripple-laminated sandstone, with small amounts of interspersed trough cross-bedded sandstone. Overall, the main sand body in outcrop displays an upward-fining succession of facies from medium to upper fine-grained trough cross-beds to fine-grained ripple-laminations. Based on the interpretation of individual facies, this upward-fining deposit is attributed to a gradual decrease in flow velocity.

STRATIGRAPHIC ARCHITECTURE

Methods

Ancient fluvial deposits exhibit a systematic hierarchy of stratigraphic relationships that can be used to improve reservoir characterization, modeling, and prediction (Sprague et al., 2003). Several authors have published methods of classifying fluvial elements (Jackson, 1975; Friend, 1983; Allen, 1983; Miall, 1985; Koltermann and Gorelick, 1996). Jackson (1975) developed a hierarchical classification of sandy bedforms scaled to process and time, which includes microforms, mesoforms, and macroforms. Microforms scale to the viscous sublayer and are sensitive to grain roughness. Examples of microforms include ripple-laminations, current lineations, and lower-stage plane beds. Mesoforms scale to the outer turbulent zone, and are more sensitive to form roughness. Dunes (planar and trough) and sandwaves are examples of mesoforms. Unlike micro- and mesoforms, macroforms are largely independent of flow conditions and respond largely to the geomorphological regime of the depositional system. In fluvial systems, this means that macroforms, such as point bars, scale to the bankfull discharge of the river. Friend (1983) took this classification scheme and applied it to field-based work, pointing out the potential pitfalls and limitations associated with identifying bedforms. Another classification system created specifically for fluvial environments (but has been applied to other environments) was developed by Miall (1985). He proposed a descriptive classification which includes the following architectural elements: channels, gravel bars and bedforms, sandy bedforms, microforms, lateral-accretion deposits, sediment gravity flows, laminated sandstone sheets, and overbank fines. Although this classification scheme has been widely used, the bedforms within each element are mixed in scale and respond to different equilibrium conditions. Koltermann and Gorelick (1996) proposed a composite classification of scales of

heterogeneity in sedimentary rocks. From smallest to largest, these scales include pore, flow-regime features, stratigraphic features, channels, depositional environments, and sedimentary basin. The flow regime and stratigraphic features are the scale of focus in this study. Jackson's terminology is used because it provides the essential link between scale and process, but insights gained from all of the described methods were taken into consideration for completeness.

Architectural Analysis

The stratigraphic framework and hierarchy of architectural elements of these deposits were used to build detailed 2-D and 3-D geologic models of the outcrops. In order to accurately describe and define architectural elements, the following details were included: 1) the nature of the lower and upper bounding surfaces, 2) external geometry, 3) scale, and 4) internal geometry (Miall, 1985). Prior to assigning these elements to specific depositional environments, the description and depositional process is first discussed herein. The stratigraphic architecture is then integrated with the facies analysis to interpret the overall environment of deposition.

The highest-order bounding surfaces present in the outcrop are those that separate macroforms. Two sandy macroforms are identified in the outcrop study area, which are encased by mudstone units (Figure 2.10). Internally, the macroforms contain meso- and microforms, which reveal local flow conditions and variations.

The oldest macroform (M-1) present is also the largest-scale macroform in the outcrop of interest. An erosional surface separates this macroform from underlying mudstone and coal facies. This surface is sharp, with a maximum relief of approximately 0.7 m (2.3 ft). M-1 consists of at least two amalgamated macroform units, a poorly-exposed older bedform (M-1a) and a younger bedform (M-1b). These

are separated by an erosional surface dipping to the south with up to 25 cm (10 in) of relief. M-1a is only visible on the northwest outcrop, while M-1b is exposed on all three outcrops. The overall geometry of the M-1 macroform is lens-shaped and the maximum thickness is approximately 7.6 m (25 ft). The lateral extent of the macroform is determined using outcrop measurements and empirical equations which are discussed in the following section on paleochannel reconstruction. Facies assemblages present in this unit are dominantly Facies A and Facies B, with lesser amounts of Facies E. These facies occur in a repeated vertical succession, from bottom to top, Facies E, Facies A, and Facies B. The dominant internal geometries present within the macroform are high-angle dipping surfaces, which are best exposed on the northwest outcrop. The average dip of the surfaces is between 10 and 12 degrees. These surfaces dip to the north in the M-1a bedform and to the south in the M-1b bedform, indicating that the macroforms accreted in opposite directions. On the east outcrop, these dipping surfaces are recognized as planar, horizontal features. The lithologies present along these dipping surfaces vary laterally within the macroform. Updip, mudstone is common along the surfaces, changing downdip to silty sandstone with common siderite concretions. Internally within the macroform, both micro- and mesoform structures (e.g. trough cross beds, ripple laminations) are present, which imply fluctuations in flow conditions (i.e. flow velocity, water depth). The upper bounding surface of the M-1 is sharp and planar with little to no relief.

Separating M-1 from the next macroform (M-2) is a mudstone interval. The lower bounding surface between the mudstones and M-2 is sharp and planar, with few undulations. This macroform is more sheet-like than M-1, but also pinches out laterally. M-2 varies in thickness from 1.5 to 3 m (5 to 10 ft) and is composed mainly

of Facies B, with lesser amounts of Facies A. Unlike M-1, there are no large-scale internal bedding features.

DEPOSITIONAL SETTING

Based on the sedimentologic and stratigraphic data and interpretations, the outcrops studied in Coal Canyon were deposited in a highly sinuous fluvial environment (Figure 2.11). This interpretation is in general agreement with those made by Lorenz (1989), Tyler and McMurry (1995), Hettinger and Kirschbaum (2002), and Cole and Cumella (2003). A general transport direction from west to east is implied from outcrop paleocurrent data, which is supported by previous outcrop measurements in this and nearby localities (Figure 2.12; Cole and Cumella, 2003).

Macroform M-1 is interpreted as a point-bar deposit, based on the presence of several important criteria, including 1) overall sand-body geometry, 2) internal architecture of the sand body, and 3) internal facies succession. Others have previously interpreted this deposit as a point bar (Cole et al, 2002, Cole and Cumella, 2003). Point bars in general have a lens-shaped, 3-D geometry, as determined by the interaction of flow and sediment transport in curved alluvial channels (Willis, 1989). The thickest part of a point bar is at the bend apex, corresponding to the deepest part of the channel. By traversing M-1 in outcrop, the sand body decreases in thickness until it eventually pinches out into the surrounding mudstone units. Point bars also tend to have sharp, scoured bases due to the nature of the helicoidal flow that controlled deposition within the bedform (Tanner, 1960). This helical pattern of flow produces a zone of reduced shear stress and where a significant amount of sedimentation can occur, allowing the channel bank to accrete laterally at a high angle to the principle flow direction (Miall, 1996). These high-angle surfaces were

first referred to as epsilon cross stratification by Allen (1963), and are today known as lateral-accretion surfaces. The internal facies arrangement within point-bar deposits has been well documented in both ancient and modern fluvial systems (Allen, 1965, 1970; Leeder, 1973; Puigdefabregas, 1973; Jackson, 1976; Collinson, 1978; Plint, 1983). In fluvial systems, both coarsening- and fining-up deposits occur, the former occurring on the upstream portion of a meander bend and the later on the downstream end. Preservation potential of fine-grained alluvium is dependent on the nature and frequency of lateral channel migration (Bridge and Leeder, 1979). The upstream portion of a point bar has a low preservation potential, and is not well represented in ancient fluvial rocks (Plint, 1983). It is therefore common to observe a fining-upward sequence within preserved point-bar deposits, which consists of an erosive-based sandstone unit (coarse member) that fines upward into fine-grained siltstones with sandstone intercalations (fine member) (Leeder, 1973). This sequence of lithologies was observed in all measured sections documented from the three outcrops.

Macroform M-2 is interpreted as a crevasse splay deposit based on the overall geometry of the sand body and the internal facies arrangement. Splays are generally sheet-like bodies tens to hundreds of meters across and 1 to 2 m (3 to 7 ft) thick (Miall, 1996). Typical facies present in splay deposits include ripple-laminated sandstone and cross-bedded sandstone, with commonly associated plant roots and bioturbation. Both upward-fining and upward-coarsening stratal deposits are present. Crevasse splays are produced when there is a break in the levee of a stream, causing sediment to be introduced to the floodplain (Miall, 1996). Deposition occurs as a result of flow expansion and loss of stream power as the discharge goes from confined to unconfined flow. These deposits are significant because they form as an intermediate step in the process of channel avulsion and abandonment.

PALEOCHANNEL RECONSTRUCTION

Paleohydraulic Interpretation

The internal geometries and grain-size distribution within point-bar deposits are controlled by the interaction of flow and sediment transport in meandering channels (Willis, 1989). Using detailed sedimentologic descriptions of facies, the paleohydraulic conditions of the depositional environment can be inferred using empirical relationships (Ethridge and Schumm, 1977). The limitations of these relationships are severe and caution should be exercised in their application (Miller et al., 1977). These relationships are typically developed through flume experiments, which are not fully representative of natural environments because: 1) the channel cross-section is rectangular, 2) the walls of a flume are straight and can not be eroded, 3) the width-to-depth ratio is typically too small, 4) the channel length is too short, and 5) the maximum flow depths attainable in flumes are at the lower end of the range of flow depths in natural streams (Middleton and Southard, 1978). In this context, the relationships are applied to extract approximations for paleoflow conditions and were not rigorously tested.

There is a unique association between bedforms and flow dynamics based on the following assumptions: 1) there is a direct relationship between bedform and hydrodynamic regime, 2) internal structures are related to the larger bedform, and 3) the bedform is in equilibrium with the flow (M. Gardner, personal communication, 2003). One major limitation of these statements is the time function relationship between the rate of growth of the bedform to equilibrium conditions and flow strength. Since flow strength is inversely proportional to bedform size (Leeder, 1999), smaller bedforms tend to reach equilibrium conditions faster and bias the preservation of these bedforms. The flow regime concept is an attempt to link bed

roughness, flow behavior, competence (grain roughness), and capacity (sediment transport rate) (Simons and Richardson, 1961).

Estimates of flow velocity are made using average grain size and the types of sedimentary structures present. Grain size in the lower portion of the point bar is approximately 0.21 mm (upper fine sand) and the dominant sedimentary structures are trough and tabular cross beds (i.e. dune bedforms). Using a traditional bedform phase diagram, which relates grain size to flow velocity, the estimated flow velocity for the lower portion of the point bar is between 65 and 80 cm/sec (26 and 31 in/sec) (Figure 2.13; Middleton and Southard, 1978). The upper portion of the point bar has an average grain size of 0.149 mm (lower fine sand) with dominantly ripple laminations. The same bedform diagram predicts flow velocities between 30 and 60 cm/sec (12 and 24 in/sec) for the upper portion of the point bar. These estimates assume a mean flow depth of 40 cm (16 in). This upward decrease in flow velocity is expected due to the upward fining of grain size and the change in scaling of sedimentary structures.

Paleochannel Morphology

The estimation of fluvial sand body size is of vital importance in determining reservoir volumetrics and hydrocarbons in place (Lorenz et al., 1985). The maximum lateral extent of a fluvial sand body is a function of the wavelength and amplitude of the meanders, which can be estimated from channel size (Collinson, 1978). Two methods of calculating paleochannel morphology were used in order to compare results and evaluate their significance. Table 2.2 summarizes the equations used for calculating the paleochannel hydraulic and morphologic characteristics and the results of both methods, referred to herein as Method A and Method B.

Method A

Ethridge and Schumm (1977) present a series of empirically derived equations based on the equations, tables, and graphs of previous authors (Schumm 1963, 1968, 1972; Leopold and Wolman, 1960; Hack, 1957; Dury, 1965). A number of hydraulic and morphologic characteristics can be computed using the following data that can be obtained from ancient fluvial rocks: 1) W (bankfull stream width), 2) D (bankfull stream depth), 3) S_c (percent silt-clay in channel bed), and 4) S_b (percent silt-clay in channel bank). Bankfull width and depth are defined as the maximum width and depth that a stream channel may attain before the discharge of floodwater into areas outside of the channel (Figure 2.14; Leeder, 1973). The variables S_c and S_b are difficult to determine without detailed petrographic and geochemical analysis, and will not be further discussed. Paleochannel width and depth can be estimated from point-bar deposits, such as the one that is the focus of this study. In order to calculate bankfull depth (D), the average thickness of the point-bar sand body (D*) is corrected for the curvature of the meander bend (versus a straight-reached channel) and compaction.

$$D = D^* \times 0.585/0.9$$

The average thickness (D*) of the younger point bar (M-1b) is approximately 7.6 m (25 ft) yielding a bankfull depth of 4.9 m (16 ft). Bankfull width (W) is calculated by assuming point bars span approximately two-thirds the distance of the channel (Allen, 1965). In outcrop, the width of the point bar is determined by averaging the horizontal width of the all of the lateral-accretion surfaces (W*).

$$W = W^* \times 1.5$$

Poor outcrop exposure often limits the availability of such measurements (Ethridge and Schumm, 1977). Fortunately, the exceptional exposure of the point bar in Coal Canyon allows for such measurements to be made. The average horizontal width of

an accretion surface (W*) is 29.6 m (97 m) and yields a bankfull width of 44.4 m (146 ft). Another method of calculating bankfull width has been developed by Leeder (1973) for use in the absence of good outcrop exposure, and will be discussed in the Method B section. Using the bankfull width and height, a number of other morphologic characteristics can be calculated, including the width-to-depth ratio (F), sinuosity (P), mean annual discharge (Q_m), mean annual flood (Q_{ma}), channel slope (S), and meander wavelength (L). The width-to-depth ratio is a simple calculation:

$$F = W/D$$

This equation results in a width-to-depth ratio of 9 for the Coal Canyon point bar. Sinuosity (P) is defined as the ratio of the channel length between two points (following the channel path) and the straight path between the same two points.

$$P = 3.5 \times F^{-0.27}$$

Application of this function to the previously calculated width-to-depth ratio equates to a sinuosity of 1.9, which is considered a moderate to highly sinuous stream. Both the mean annual discharge (Q_m) and the mean annual flood (Q_{ma}) are calculated using bankfull channel width and the width-to-depth ratio.

$$Q_m = W^{2.43}/18F^{1.13}$$

$$Q_{ma} = 16(W^{1.56}/F^{0.66})$$

These equations yield a mean annual discharge and flood of 46.8 and 1395.2 cubic meters per second (cms) (1653 and 49,271 cubic feet per second [cfs]), respectively. By comparison, the discharges of several well-known river systems of the world include 180,000 cms (Amazon), 17,545 cms (Mississippi), 168 cms (Colorado), and 82 cms (Rio Grande) (River Systems of the World, 2004). Maximum discharge controls a stream's overall channel shape and cross-sectional area (Swanson, 1993). Channel slope (S) plays a major role in determining flow velocity of the

stream, which dictates the nature and type of sedimentary structures that will form. Slope is calculated using the width-to-depth ratio and bankfull channel width.

$$S = 30(F^{0.95}/W^{0.98})$$

Estimated channel slope using the point-bar outcrop data is 5.9 m/km, which is equivalent to 0.33 degrees. Meander wavelength can be estimated using several methods which relates wavelength to parameters such as the width-to-depth ratio, bankfull width, and mean annual discharge. The following equations were used to estimate meander wavelength (Leopold and Wolman, 1960; Carlston, 1965; Schumm, 1972) respectively:

$$L = 18(F^{0.53}W^{0.69})$$

$$L = 10.9 \times W^{1.01}$$

$$L = 106 \times Q_m^{0.46}$$

Using the previously calculated parameters and applying these equations, meander wavelength was estimated to be 789 m (2,589 ft), 503 m (1,650 ft), and 622 m (2,041 ft), respectively.

Method B

Due to the often poor exposure of point-bar outcrops, it is difficult to estimate bankfull width of the channel (Ethridge and Schumm, 1977). In high sinuosity rivers (i.e. P > 1.7), there exists a relationship between bankfull depth and width, where width increases faster than depth (Leeder, 1973).

$$W = 6.8 \times D^{1.54}$$

Using this relationship and the corrected bankfull depth from outcrop, the estimated bankfull width is 80 m (262 ft). This value is 56% larger than the previously calculated bankfull width of 44 m (146 ft), using the horizontal extent of the lateral-accretion surfaces. Using this value for bankfull width, the same equations are

applied to estimate the width-to-depth ratio, sinuosity, mean annual discharge, mean annual flood, channel slope, and meander wavelength. The resulting parameters are listed in Table 2.2 and compared with the values using Method A. The most significant parameter in this study, meander wavelength, resulted in values of 1,609 m (5,279 ft), 906 m (2,972 ft), and 881 m (2,890 ft) based on the equations of Schumm (1972), Leopold and Wolman (1960), and Carlston (1965), respectively.

Discussion

Paleochannel reconstruction is significant when attempting to build a 3-D model of a fluvial sand body. It is especially important when these estimates are used to predict reservoir geometry and size in the subsurface.

Several authors have attempted to estimate sand body extent within the Williams Fork Formation. Lorenz et al. (1985) used the empirical equations presented in Method B to determine sand-body width in the Mesaverde Group. They calculated meander wavelengths of 350 to 520 m (1,148 to 1,706 ft) and 430 to 650 m (1,411 to 2,133 ft) from core and outcrop data, respectively. Bridge and Tye (2000) revisited these estimates and determined an average meander belt width of 1,184 m (3,885 ft). This increase in meander wavelength is based on interpreting a sand body as a single channel-bar fining-upward sequence versus the three stacked point-bar deposits interpreted by Lorenz et al. (1985). The meander wavelengths calculated for the Coal Canyon point bar using the various methods presented varies between 502 and 1609 m (1,647 and 5,279 ft) with an average of 885 m (2,904 ft). Results from Method A range between 503 and 789 m (1,650 and 2,590 ft), with an average of 638 m (2,090 ft). Method B produced a range of meander wavelength between 881 and 1609 m (2,890 and 5,280 ft), with an average of 1132 m (3,710 ft). These estimates correspond well to those presented by Lorenz et al. (1985) and

Bridge and Tye (2000). The results of Method A provide estimates of meander wavelength that are more directly related to outcrop parameters, and are therefore more specific to this point bar. These estimates are applied to build a 3-D geologic model of the point bar exposed in outcrop.

CHAPTER THREE

TWO-DIMENSIONAL OUTCROP MODELING

MODELING OBJECTIVES

Geologic modeling of high-resolution outcrops is useful to identify the types and scales of heterogeneity that affect fluid flow and storage in the context of architectural, petrophysical and fluid properties (Joseph et al., 2000; Sullivan et al., 2000; Willis and White, 2000; Dalrymple, 2001; Stephen et al., 2001). There have been numerous studies that explore geologic modeling of fluvial reservoirs, including process-based (Allen, 1978; Leeder, 1978; Bridge and Leeder, 1979; Bridge and Mackey, 1993; Mackey and Bridge, 1995), stochastic (Hirst et al., 1993; MacDonald and Halland, 1993; Tyler et al., 1994; Jones et al., 1995; Eschard et al., 1998; MacDonald et al., 1998; Dalrymple, 2001), deterministic (Stephen and Dalrymple, 2003), and combination stochastic-deterministic models (Novakovic et al., 2002; Patterson et al., 2002). Many of these studies investigate stratigraphic architecture (i.e. sand-body dimensions and distribution) and reservoir connectivity on a field scale, but do not address the potential affect of internal sand-body heterogeneities (Weber, 1982).

Two-dimensional modeling of the northwest outcrop in Coal Canyon was conducted to quantify stratigraphic heterogeneities within a fluvial point-bar deposit. Both deterministic and stochastic modeling techniques were applied. Sedimentologic data collected from outcrop were used to build deterministic lithology and grain-size models, which serve as a constraint for petrophysical modeling. Four methods of distributing petrophysical properties were investigated (two deterministic and two stochastic). Porosity and permeability models were used to conduct volumetric calculations and streamline flow simulations. The streamline simulations

compare the effects of stratigraphic heterogeneity (i.e. lithology and grain-size models) and petrophysical distribution on breakthrough time, volume swept at breakthrough time, and sweep efficiency. All models were built using Roxar's IRAP-RMS software (Appendix B). A goal of this outcrop study was to provide quantitative information for use in analog studies.

MODELING FRAMEWORK

Lidar Data

In the past, quantification and modeling of outcrops was a lengthy process of correcting photomosaics and digitizing data that often did not provide adequate representation where lithology and stratigraphy showed significant 3-D complexity (Jennette et al., 2003). Gathering accurate quantitative outcrop data is difficult with photogrammetric methods where obliquity distorts the image and overlapping areas produce inconsistency in scale (Caracuel et al., 2000). It is essential in quantitative outcrop modeling to have a well-defined coordinate system in order to accurately estimate variation in rock properties (Willis and White, 2000).

The "reservoir" model framework was built using high-resolution lidar data and interpretations. Lidar is an acronym for LIght Detection And Ranging, which uses a low energy laser and sensitive receiver to acquire detailed digital elevation models of the outcrop (Jennette et al., 2003). Light-ranging and light intensity data are combined to generate 3-D outcrop models with near zero distortion in x-y-z space with centimeter-scale vertical and meter-scale horizontal resolution. This data is collected at a rate of 2,000 points per second using a pulsed laser operating at 25 kHz (Bellian et al., 2002). In this study, lidar data have been used to interpret key stratal surfaces, enhance 3-D visualization of the modeling area, and provide a straightforward method of constraining 2-D and 3-D models to the outcrop.

Lidar Acquisition, Processing and Interpretation

Lidar data of the three outcrop faces were collected on May 23, 2003 using the Texas Bureau of Economic Geology's (BEG) Optech Ilris ground-based 3-D laser scanner (Figure 3.1). Seventeen scans provide near-complete coverage of the outcrops, and were taken from five different vantage points within the canyon (Figure 3.2).

A workflow developed by the BEG was used to process and interpret the lidar images of the Coal Canyon point-bar outcrop (Figure 3.3). Initial processing of the lidar data was conducted by the BEG, and included merging the 17 individual scans into two continuous point-clouds, one on the east side and one on the west side of Coal Canyon Road. A point-cloud is a textured elevation model in 3-D space. Merging of the point-clouds was completed using IMAlign, part of the Innovmetric Polyworks software package.

Using decimated data from the lidar intensity images, a virtual reality modeling language (VRML) file was created for 3-D visualization of the outcrop surface (Figure 3.4 and Appendix C). Although the VRML does not provide the level of detail as seen in the point-cloud data, it is most useful for fast visualization of the outcrop surface and requires a minimal amount of computing power.

Interpretation of the digital lidar images was completed using IMInspect in Polyworks. Both point-cloud and intensity images were used during the interpretation process, along with outcrop photomosaics for comparison and reference. The stratigraphic architecture discussed in the previous chapter was digitized onto the outcrop surface. First, the major bounding surfaces were identified and interpreted on the point-cloud image. These surfaces include the base and top of the point-bar deposit, the base and top of the splay sandstone, and the basal coal. Next, the internal surfaces (e.g. lateral-accretion surfaces, erosional surfaces) within

the point bar were defined. The interpreted surfaces were saved as point data that were used to build the modeling framework (Figure 3.5).

Grid Construction

The framework for the 2-D models of the northwest outcrop was created using the interpreted lidar data. Point data from interpreted surfaces was imported into GeoPLUS's Petra software and 2-D grids of the surfaces were generated. These grids were imported into RMS, and the interpreted framework was projected onto a vertical 2-D plane, at the approximate location of the actual outcrop. The modeling grid was built using an XY regular grid format, which maintains constant cell width and length. Subgrids divide the model into zones that can have different grid styles and resolution and allow properties within each subgrid to be modeled separately. For the northwest outcrop model, these subgrids were defined using the stratigraphic framework. Using a grid that follows the major bedding surfaces is advantageous because beds define a natural scale for rock subdivision and depositional processes tend to align rock variations along or orthogonal to bedding surfaces (Willis and White, 2000). Cell layering is truncated at the top of each architectural element. The cell dimensions were chosen to capture the lateral and vertical heterogeneity observed in outcrop.

The architectural complexity of the northwest outcrop is reflected in the model framework by the thirteen subgrids defined by each interpreted stratigraphic surface (Figure 3.6). The total number of cells in the model is 75,900. Cell dimensions are 1.13 m by 1.5 m (3.7 by 4.9 ft) with a thickness 5 cm (2 in). The rotation angle of the grid was set such that the cell length was parallel to the outcrop face.

LITHOLOGY MODELING

Methods

Deterministic modeling methods were used to construct lithology models for the northwest outcrop. For simplicity, the lithologies modeled include sandstone and shale. Any lithology with an average grain size less than 0.0625 mm (0.002 in) was considered shale (e.g. silt and clay grain sizes), while any lithology with an average grain size greater than or equal to 0.0625 mm (0.002 in) was considered sandstone (e.g. from lower very fine sand). Lithology is a discrete parameter, and shale was assigned a value of zero and sandstone a value of one. For the models, lithology pseudo-wells were generated based on measured section data. The northwest outcrop model incorporates twenty pseudo-wells with an average spacing of 5.7 m (18.7 ft), which provides additional constraints for the interpolation of lithology within the model.

The algorithm used for distributing lithology throughout the outcrop models was an interpolation function, which is based on a weighted-average calculation, similar to another well-known interpolation technique called moving average (Roxar, 2003a). This function searches for all well data within an interpolation ellipsoid, which is defined by the influence radii and the interpolation orientation. The radius of influence used was 50 m (160 ft) and the orientation of the ellipsoid was set parallel to the outcrop face. Next, the algorithm calculated the weight of all well data points based on the distance from the data point to the center of the interpolation ellipsoid. Those data points nearest to the center of the ellipsoid were given the highest weights. A cell value is then assigned based on the weights and well data points. This process is repeated for all defined cells within the model. The interpolation algorithm produces a continuous function, with values within the range of the input data (i.e. between 0 and 1). In order to transform the interpolated values back to a

discrete parameter, the data was filtered based on subgrid and the correct lithology value was assigned to each cell.

Results

Three lithology models were generated for the northwest outcrop (Table 3.1, Figure 3.7). These models represent various levels of internal heterogeneity within the point bar, while the surrounding units (i.e. floodplain mudstones and crevasse splay) remain constant. Lithology Model 1 (LM-1) consists of 100% sand within the point bar. Lithology Model 2 (LM-2) contains 97.6% sand and 2.4% shale. The shales are distributed along the nine lateral-accretion surfaces that were identified in outcrop. Lithology Model 3 (LM-3) contains 98.8% sand and 1.2% shale. In this model, the shales are restricted to the upper portions of the lateral-accretion surfaces.

Discussion

LM-1 represents a homogeneous point bar. This model assumes that there are no internal lithologic changes within the point bar, and it is effectively modeled as a continuous sand sheet. Field-scale geologic modeling of fluvial reservoirs often uses this type of distribution within individual sand bodies. Horizontal flow within a reservoir can be hindered by shale drapes inclined to the average bedding-plane direction, having a negative influence on recovery efficiency (Weber, 1982). Continuous shales can compartmentalize reservoirs into separate hydraulic units, while discontinuous shales can create a tortuous path for fluid movement (Haldorsen and Lake, 1984). LM-2 considers that within the point bar, there are shales that effectively act as baffles. The lateral-accretion surfaces represent the most significant stratigraphic baffles, and in this scenario, are modeled as continuous

baffles across the point bar. The shale drapes are restricted to the topographically higher parts of the accretion slope, while sand on sand contacts are present further down slope. The sand on sand contacts may act as fluid baffles due to the presence of siderite nodules and siltstone intercalations documented in outcrop. LM-3 assumes that only the shale-draped portion of the lateral-accretion surfaces will act as a baffle to flow, and not the sand-on-sand contacts present in topographic lows. This final lithology model is the closest approximation of the actual lithologies present in outcrop.

GRAIN-SIZE MODELING

Methods

Grain size within the point-bar deposit was modeled using deterministic methods. Grain-size well logs were created within the modeling framework at the same location as measured sections collected in the field. The median grain size corresponding to each size classification (e.g. medium sand = 0.297 mm [0.01 in]) was recorded as the grain-size value. In addition to the five grain-size logs taken from outcrop data, another five pseudo-wells were created to help guide the interpolation. The same interpolation function previously described for lithology modeling was also employed to distribute grain size throughout the model.

Results

The resulting grain-size model of the northwest outcrop ranges from 0.03 mm to 0.297 mm (0.001 to 0.01 in), with an average grain size within the point bar of 0.19 mm (0.007 in); classified as silt, medium sand, and fine sand, respectively (Figure 3.8). Laterally, grain size has a correlation length of approximately 10 to 30 m (33 to 98 ft), while the vertical correlation length is from 0.2 to 1.0 m (0.7 to 3.3 ft), which is

based on observations made from outcrop. These correlation lengths are useful for defining the variogram range during petrophysical modeling because grain size has a significant control on petrophysical properties (Beard and Weyl, 1973). In general, grain size exhibits a fining-upward trend on the scale of individual accretionary units and the entire point-bar deposit.

Discussion

Outcrop measurements reveal two scales of fining-upward grain size, the first being the overall point-bar deposit as well as within each individual lateral-accretion unit. These two scales were preserved in the outcrop grain-size model. This model provides a more realistic and complex portrayal of internal heterogeneity when compared to the previously described lithology models. Grain-size models may also offer an alternative to detailed facies modeling, assuming that these data exist, since the sedimentary structures that define many facies classifications are inherently linked to grain size.

PETROPHYSICAL MODELING

Modeling Scenarios

Porosity and permeability are the two main variables needed for reservoir characterization (Deutsch, 2002). Both stochastic and deterministic methods were applied in generating petrophysical models, using the lithology models and the grain-size model as constraints. The spatial variability of petrophysical properties can have a significant affect on reservoir performance. Four methods were used to assess the affect of various distributions of petrophysical properties on fluid flow. These four methods include: 1) a uniform distribution, 2) a conditionally simulated distribution, 3) a conditionally simulated distribution with an imposed depositional

trend, and 4) a distribution related to grain size (Table 3.2). To be consistent between the models, the same porosity to permeability transform was used, which will be described in the permeability modeling section. The uniform distribution assumes that all of the sand in the model has a porosity of 9.0% and a permeability of 192 md. These values were chosen because 9.0% represents the median value for the given range of productive sandstone porosities (6 to 12%). The permeability value is a result of the transform applied to all porosity data to obtain permeability. Shale was assigned values of 1.0% for porosity and a permeability of 0.1 md. The conditionally simulated models were generated using a geostatistical algorithm and constrained with an input histogram and variogram. A linear depositional trend was incorporated with the conditional simulation to produce a fining-upward trend in porosity and permeability. The petrophysical models related to grain size were generated using a simple grain size to porosity and porosity to permeability transforms. Table 3.3 explains the naming convention for the resulting petrophysical models. More detailed descriptions of petrophysical modeling methods are discussed in the following two sections.

Porosity Modeling

Methods

Average porosities for productive sandstones within the Williams Fork Formation range from 6 to 12% (Cumella and Ostby, 2003). This porosity distribution for sand was honored in all four porosity modeling scenarios. Shale was assigned low values of porosity (0.1 to 1.0%), such that this lithology would act as a flow baffle rather than a barrier. Each of the four distribution scenarios required different steps to generate the porosity models.

For the uniformly distributed porosity model, the median value of 9.0% was chosen for sand lithologies. Shale porosity was set anomalously low to 1.0%. The three lithology models were filtered separately based on sand and shale values and the correct porosity value was assigned to a pre-defined parameter.

For the stochastic models generated by conditional simulation, a normally distributed input histogram was used to constrain porosity within the model. Although the input porosity data was already normally distributed, a series of transformations were applied to the data. Data transformations are used because they: 1) remove all outliers, 2) meet the assumption of modeling algorithms that data has a Gaussian distribution, and 3) account for various trends in the data (Deutsch, 2002). First, all porosity data and realizations were truncated between 0.1 and 12.5%. For the conditionally simulated models with fining-upward porosity, the next step was to apply a depositional trend. This transformation uses a linear function in stratigraphic depth to impose a fining-upward trend within the reservoir zone. The final transformation applied in both stochastic modeling scenarios was a normal-score transform, where the reservoir residuals are assumed to be distributed according to the probability density function, resulting in a Gaussian distribution with a mean of zero and a standard deviation of one (Roxar, 2003b). The variogram is a useful tool for investigating and quantifying the spatial variability of petrophysical properties (Gringarten and Deutsch, 2001). Spatial correlation of porosity was modeled with a spherical function for the model variogram. Variogram ranges for the horizontal and vertical direction were 20 and 1 m (66 and 3.3 ft), respectively (Figure 3.9). These ranges were determined using the correlation lengths of the previously described grain-size model. The algorithm used to generate the stochastic porosity models is a Fast Fourier Transform (FFT), which performs the convolution of a white noise field with a filter to create the correct correlation structure (Roxar, 2003b). The

simulation procedure involves performing unconditional simulation of a spatial variable Z(x) (e.g. porosity or permeability) that is normally distributed with a variogram γ(h) and then performing kriging on the unconditional simulated field.

Grain size and sorting are the primary textural controls on porosity and permeability in clastic rocks (Beard and Weyl, 1973). A simple linear transform was applied to the grain-size model to compute porosity, correlating maximum grain size with maximum porosity and minimum grain size with minimum porosity. The following equation was used for the transform (Figure 3.10):

$$\Phi = 0.4167*(\text{grain size in mm}) - 0.0037$$

The lithology models were not used as a constraint in this deterministic method. Because only sand and shale are represented in the lithology models, grain-size variations are representative of the two lithologies as they are distributed in LM-3, which is the closest approximation to the actual outcrop.

Results

Ten porosity models were generated based on the four petrophysical distributions and conditioned using the three lithology models. Porosity distribution scenarios are shown together for visual comparison in Figure 3.11. Statistical data for all porosity models are compiled in Appendix D.1.

The porosity models with a uniform distribution are U-1, U-2, and U-3 (Figure 3.12). Model U-1 has a single value of porosity within the point-bar deposit, equal to 9.0%. This model was constrained by LM-1, the homogeneous point-bar scenario. Model U-2 has an average porosity of 8.8% within the point bar, with a minimum and maximum porosity of 1.0% and 9.0%, respectively. This decreased average porosity is due to the presence of continuous shale drapes on the lateral-accretion surfaces, as defined in LM-2. Model U-3 has an average porosity of 8.9% and a 1.0%

minimum and 9.0% maximum porosity. In this model, shale porosities are confined to the upper portion of the lateral-accretion surfaces, conditioned using LM-3. These models represent the simplest spatial distribution of porosity out of all the distribution scenarios that were tested.

Three porosity models were stochastically generated using conditional simulation, including CS-1, CS-2, and CS-3 (Figure 3.13). Spatial continuity of porosity in these models is controlled by the input variograms. Model CS-1, conditioned to LM-1, has an average porosity of 8.9%, with a minimum porosity of 5.0% and a maximum porosity of 12.0%. The average porosity of model CS-2 is 8.7%, with 0.01% and 12.0% as the minimum and maximum porosities and was conditioned using LM-2. Model CS-3, conditioned using LM-3, has an average porosity of 8.8%, with 0.01% and 12.0% as the minimum and maximum porosities. These models, in comparison to the other three scenarios, have the most random distribution of porosity.

Using a conditional simulation with a fining-upward linear trend produced models CST-1, CST-2, and CST-3 (Figure 3.14). Model CST-1, conditioned to LM-1, has an average porosity of 9.5%, with a minimum porosity of 6.7% and a maximum porosity of 12.5%. Model CST-2 has an average porosity of 9.3%, with a minimum and maximum porosity of 0.3% and 12.5%, respectively. This model was conditioned using LM-2. Model CST-3, conditioned with LM-3, has an average porosity of 9.4% with minimum and maximum porosities of 0.3% and 12.5%. The fining-upward trend in porosity follows the grid cell layering, causing the stratigraphically lower portions of the point bar to have the highest porosities. In this case, the highest porosities are on the northern end of the outcrop model.

The grain-size model was transformed to create a single porosity model based on grain size (Figure 3.15). The average porosity in this model is 7.6%, with a

minimum of 0.8% and a maximum of 12.0%. Spatial continuity of porosity in this model is the highest compared to the two stochastically generated porosity scenarios.

In general, the conditionally simulated models with linear trends have the highest values of porosity, the lowest average porosity is association with the grain-size model. When comparing models using the same type of distribution, those conditioned using LM-1 have the highest porosities, while LM-2 conditioned models have the lowest porosities. Correlation length of porosity is greatest in the grain-size models (excluding the uniform models).

Discussion

Models generated with a uniform porosity distribution are a drastic oversimplification of the internal petrophysical heterogeneities present within the point bar. If a uniform distribution method must be applied, constraining the result to a more realistic lithology model (e.g. LM-2 or LM-3), will improve the accuracy of the porosity model.

The conditionally simulated porosity models are a definite improvement over the uniformly distributed models. These models not only incorporate lithologic variability, but also account for the spatial variability of petrophysical properties within a single lithology. This variability may be due to the presence of sedimentary structures (e.g. trough cross-beds, ripple laminations), bioturbation, diagenesis, or fracturing. Yet, these models are still not truly representative of the outcrop. The conditionally simulated models contain pod-like bodies of high porosity, whose placement is stratigraphically random, controlled only by the input histogram and estimated variogram. The conditional models with an imposed stratigraphic trend produce the recognizable fining-upward sequence that is common within point bars.

Due to the trend following stratigraphic depths (i.e. time lines), facies tracts are cross cut. The high porosities should be distributed at the depositional base (i.e. the lowest part of the channel) of each lateral-accretion unit, not along the entire stratigraphic surface.

The single porosity model generated based on grain size represents the closest approximation to the actual outcrop. This model incorporates lithologic and petrophysical variability that follows implied facies-tract boundaries. Future application of this method of modeling porosity may have significant advantages over more traditional methods, assuming adequate data are available to conduct grain-size modeling.

Permeability Modeling

Methods

The Williams Fork Formation produces mainly from fracture permeability in the subsurface, due to the low matrix permeability, which is on the order of 0.1 to 2 μd (Cumella and Ostby, 2003). In order to efficiently run streamline simulations using the modeling results, a reservoir analog was chosen to populate the outcrop models with permeability.

The Brent Group is a Middle Jurassic reservoir in the northern North Sea. The Ness Formation, a part of the Brent Group, was deposited as a complex of coastal and deltaic sediments, including isolated, fining-upward fluvial channels, coal seams, and lagoonal mudstones (Richards, 1992). The Brent Group provides a reasonable subsurface analog for the Williams Fork Formation outcrops in western Colorado.

Core plugs from productive sandstones of the Brent Group were analyzed for porosity and permeability by Stiles and Hutfilz (1992) and later compiled by Nelson

and Kibler (2003). When plotted together, porosity and permeability show a log-normal relationship that can be described using the following equation:

$$k = 0.1227 * e^{0.3199\Phi}$$

Porosities from this data set range from 18.0 to 28.0%, which are significantly higher than porosities observed in the Williams Fork Formation. Therefore, the porosities were shifted by 14.0% to better capture the range of porosities found in the Williams Fork, yielding the following equation that was used to transform sandstone porosity to permeability in the models (Figure 3.16):

$$k = 10.811 * e^{0.3199\Phi}$$

A separate equation was used to transform shale porosity to permeability.

$$k = 0.05* e^{0.3199\Phi}$$

In order to generate the permeability models, each porosity model was filtered separately to sand and shale, based on one of the three lithology models. The appropriate transform was then applied and the filter removed. Although only a single porosity model based on grain size was computed, three permeability models were produced using this method.

Results

Twelve permeability models were generated using the described transforms. This method of generating permeability models by transformation of porosity models results in a direct correlation of porosity and permeability models. Permeability scenarios are shown together for visual comparison in Figure 3.17. Statistical data for all permeability models are presented in Appendix D.2.

Permeability models with a uniform distribution, U-1, U-2, and U-3 were generated using their correlative porosity models (Figure 3.18). Within the point bar, model U-1 has a single permeability value of 192 md. Model U-2 has an average

permeability of 187.5 md, with minimum and maximum permeability values of 0.06 md and 192 md. Model U-3 has an average permeability of 189.7 md, with 0.06 md and 192 md as the minimum and maximum permeabilities.

Three permeability models, CS-1, CS-2, and CS-3 were created using the conditionally simulated porosity models (Figure 3.19). Model CS-1 has a range of permeabilities from 73.5 to 503 md, with an average of 222.9 md. Model CS-2 permeabilities ranged from 0.05 to 503 md, averaging 215.8 md. Model CS-3 has an average permeability of 216.6 with a minimum and maximum permeability of 0.05 md and 503 md, respectively.

Permeability models CST-1, CST-2, and CST-3 were generated from the conditionally simulated porosity models with a fining-upward trend (Figure 3.20). Model CST-1 has an average permeability of 238 md, with a minimum and maximum of 90.7 and 586 md, respectively. Model CST-2 had a range of permeabilities from 0.05 to 586 md, with an average of 232. Model CST-3 has an average permeability of 234 md, with a minimum of 0.05 md and a maximum of 586 md.

Using a single porosity model, three lithology models, and two transform equations, three permeability models, GS-1, GS-2, and GS-3 were generated based on grain size (Figure 3.21). Model GS-1 has an average permeability of 164.9 md, with minimum and maximum values of 14.3 and 503 md, respectively. Model GS-2 has a range of permeabilities between 0.07 and 503 md, with an average of 161.8 md. Model GS-3 has an average permeability of 164.4 md, with a minimum of 0.07 md and a maximum of 503 md.

The general visual trends observed when comparing the permeability models are that same as those observed with the porosity models. Of the petrophysical distribution methods, the conditionally simulated models with a linear trend exhibit the highest overall permeability while the grain-size models have the lowest

(maximum difference 33%). Of the lithology models, LM-1 has the highest permeability while LM-2 has the lowest. The grain-size models also have the highest continuity (excluding the uniform distribution) compared to the lower continuity observed in the conditionally simulated models.

Discussion

Since the permeability models were derived directly from the porosity models, these models exhibit similar characteristics. Unlike the case with porosity, three permeability models were generated based on the grain-size model porosity. All of these models are potentially representative of the actual distribution of permeability in a point bar. The three models account for the lateral and vertical changes in lithology, but vary in the method of assigning permeability to shale lithologies.

VOLUMETRICS

Methods

Volume estimates were calculated on the resulting outcrop models to provide a general comparison of potential drainable volumes, the degree of reservoir compartmentalization, and pore volume for the various modeling scenarios. Drainable volume calculations assumed that all sand lithologies are drainable that are in contact with another drainable grid block. This parameter was computed for the entire reservoir (i.e. bulk volume of sand), and for the volume drained by three separate producing wells, one placed on the southernmost end (Well A), one in the center (Well B), and one on the northernmost edge of the model (Well C). The results of this calculation reveal the amount of compartmentalization within each lithology model and what compartments are drained based on the placement of the

producing well. Pore volumes were calculated using the bulk volume of the point bar and each of the ten porosity models.

$$V_{pore} = V_{bulk} * \Phi$$

The results of the pore volume calculations were also used to calculate the volume of the reservoir swept during streamline simulation.

Results

Since LM-1 is composed of only sand lithologies with no internal heterogeneities, the entire volume of the point-bar reservoir is drained regardless of well placement, resulting in a total volume of 1,886 m^3 (66,600 ft^3) (Figure 3.22). LM-2 has a bulk sand volume of 1,840 m^3 (65,000 ft^3) and includes ten reservoir compartments (Figure 3.23). Well A drained two of the compartments with a total volume of 703 m^3 (24,800 ft^3), Well B drained three of the compartments totaling 1,186 m^3 (41,900 ft^3), and Well C drained four compartments totaling 438 m^3 (15,500 ft^3). LM-3 has a bulk sand volume of 1,863 m^3 (65,800 ft^3) with four reservoir compartments (Figure 3.24). Well A drained one compartment with a total volume of 1,768 m^3 (62,400 ft^3), Well B drained the same compartment totaling 1,768 m^3 (62,400 ft^3), and Well C drained four compartments totaling 438 m^3 (15,500 ft^3). A summary of drainable volumes and reservoir compartmentalization is presented in Table 3.4.

Pore volume was computed for each porosity model and is summarized in Table 3.5. When comparing distribution methods, the conditionally simulated models with a fining-upward trend have the highest pore volume and the grain-size models have the lowest pore volume. Comparing the lithology models (for all distributions except the single grain-size porosity model), as expected, LM-1 has the highest pore volume and LM-2 has the lowest pore volume.

An analysis of variance (ANOVA) test was performed on the resulting pore volume results to assess the statistical significance between the modeling scenarios (Appendix E.2 to E.4). ANOVA is a statistical test for heterogeneity through the analysis of group variances. This method calculates a probability value (p-value) and a Fisher ratio (F-ratio). If the F-ratio is greater than the critical F-value, then the null hypothesis can be rejected that all the means are the same for the different groups (Box et al., 1978). The p-value indicates the probability that the result is actually random; therefore the magnitude of the p-value is used to determine the significance of the result (Appendix E.1). This analysis was performed using an online program which calculates the p-value and f-ratio for a given set of input data (http://www.physics.csbsju.edu/stats/anova.html). A comparison of the pore volumes between lithology models results in accepting the null hypothesis (F-ratio [0.4313] < F-critical [5.143]), implying that the pore volumes for each lithology model are not significantly different. Analysis of the petrophysical distribution leads to rejecting the null hypothesis (F-ratio [170.5] > F-critical [4.066]), meaning that there is a significant difference in pore volume between the four distribution methods. The low p-value (0.000) indicates that the difference between the models is highly significant and not a random result.

Discussion

These volumetric calculations have implications for the reservoir management and drilling program strategy in a subsurface field. Understanding the amount of reservoir compartmentalization is essential for vertical or horizontal well placement. For example, if continuous baffles are present within the point bar, as is the case with LM-2, greater volumes will be drained if the producing well is placed in an area of low stratigraphic complexity, but not so low that the well misses a large

number of the compartments. In the case of a reservoir with discontinuous baffles, such as LM-3, well placement did not have a large affect on drainable volume, but a small increase was observed when the well was placed in the most stratigraphically complex area. As an alternative to vertical well placement, a horizontal well drilled nearly perpendicular to paleoflow would drain the majority of the reservoir. This type of drilling plan would be especially useful in the case of continuous barriers or baffles within the reservoir.

Pore volume did not vary appreciably between the lithology models. This is a result of the low bulk volume (< 3%) of the shales in all three models. The distribution method does have a significant affect on the resulting pore volume of the model. Pore volume is directly related to porosity within the model. The conditionally simulated models with an imposed trend have the highest pore volumes because the overall porosity is higher in these models.

STREAMLINE SIMULATION

Methods

In order to quantitatively assess the affect of lithologic and petrophysical distribution on fluid flow within a point-bar reservoir, streamline simulation was conducted on the resulting outcrop models. Fluid flow was estimated using the *RMSstream* module in IRAP-RMS, which is based on single-phase streamline simulation. A streamline is defined as the trajectory of a moving fluid particle or a line of equal velocity (Pollack, 1988). Input parameters for streamline simulation include permeability (vertical and horizontal, used to calculate transmissibility) and porosity models, rock and fluid compressibility, fluid viscosity, reference depth and pressure, fluid rate (minimum for producer and maximum for injector), injector bottom-hole pressure, and producer bottom-hole pressure. These parameters were

set assuming subsurface conditions (Table 3.6). Vertical permeability (z-direction) was scaled to 10% of the original permeability models. All parameters were held constant between the various simulations.

An injection well was placed on the south (left) side of the model with the producing well on the north (right) side. Both wells penetrate the entire thickness of the model. Only sand lithologies were open to flow in the injection and production wells.

Results

Twelve streamline simulations were completed using the previously described porosity and permeability models. Both quantitative and qualitative comparisons were made using the results of the simulations. Calculated parameters from the streamline simulations include breakthrough time, volume swept at breakthrough time, and sweep efficiency, which are summarized in Table 3.7.

Breakthrough time (BTT) is the amount of time it takes for a fluid particle to travel through the model from an injection well to a production well (Figure 3.25). In addition to simply comparing BTT, the simulation results were compared by displaying the time from injector (TFI) at BTT for each modeling scenario (Figures 3.26, 3.27, 3.28 and 3.29). This reveals the preferential path of the fluid front for qualitative comparison.

In general, BTT in the models with a uniform distribution or constrained to LM-2 were longest, while those with the grain-size distribution or constrained to LM-3 were the shortest. Comparing the percent change of BTT between the lithology models, using LM-1 as the standard, BTT for LM-2 differs by an average of 30.7% and for LM-3 by 23%. Comparison of the distribution methods, using the uniform distribution as the standard, shows a 7.7% BTT difference in the conditional

simulation models, an 18.8% difference for the conditionally simulated models with a trend, and a 59.7% difference for the grain-size models.

An analysis of variance (ANOVA) was conducted on the resulting BTT data to assess the statistical significance of the results (Appendix E.5 to E.7). Based on the analysis of the three lithology models, the null hypothesis was rejected (F-ratio [24.43] > F-critical [5.143]), indicating that the average BTT for each lithology model is significantly different. The small p-value (0.001) suggests that the variance observed is highly significant and not a result of random factors, especially when the grain-size modeling results are not considered (because all the grain-size models account for the lithology to begin with). When comparing BTT between the petrophysical distributions, the null hypothesis was accepted (F-ratio [2.148] < F-critical [4.066]), suggesting that the petrophysical distribution does not have affect BTT.

Volume swept is defined as the volume of the reservoir that is touched by the injected fluid, and in this case, at BTT (Figure 3.30). The sweep efficiency is the fraction of the floodable pore volume that is swept by the injected fluid. The calculation of pore volume was described in the previous section on volumetrics.

LM-1 has the highest sweep efficiency when compared to the other lithology models, while LM-3 has the lowest sweep efficiency. The average percent change in volume swept compared to LM-1 is 9.5% for LM-2 and 25.4% for LM-3. Comparing the petrophysical distributions, the uniform models show the highest sweep efficiency (in 2 out of 3 cases) while the grain-size models have the lowest efficiency. The average percent change in volume swept, using the uniform model as a standard, results in a 5.5% difference for the conditionally simulated models, 3.2% for the conditionally simulated models with a trend, and 43.9% for the grain-size models.

ANOVA was also conducted using the volume swept calculated for each model (Appendix E.8 to E.10). When comparing lithology models, without including the results from grain-size modeling, the null hypothesis was rejected (F-ratio [98.51] > F-critical [5.143]) indicating that volume swept is significantly different between the three lithology models. The p-value (0.000) indicates a highly significant result that is not random. Comparison of the petrophysical distributions leads to a rejection of the null hypothesis (F-ratio [5.407] > F-critical [4.066]), meaning that the average volume swept for the four distribution methods are different from each other and a moderate p-value (0.025) indicates that the result is not likely due to a random event.

The character of the fluid front varied most significantly between the three lithology models. LM-1 exhibits a uniform fluid front, such that a large percentage of the fluid front is close to the production well at BTT. LM-2 shows a uniform fluid front through the early stages of injection, but as the front nears the production well, the fluid chooses a preferential flow path. LM-3 has a non-uniform front in which the fluid interfingers within the model, concentrated mainly at the base of the point bar. When comparing the fluid front in the four petrophysical distributions, the uniform models also exhibit the most uniform fluid front. The two conditionally simulated models both show a degree of interfingering at a scale smaller than the overall fluid front. The grain-size models display a super-concentrated fluid front at the base of the point bar, with much of the upper portion of the reservoir remaining unswept.

Discussion

The results of the streamline simulations reveal the magnitude of the effect that internal lithologic and petrophysical heterogeneity has on fluid production from a point-bar reservoir. This heterogeneity explains the low recovery efficiency often observed in fluvial reservoirs (Hartkamp-Baker and Donselaar, 1993).

Comparison of BTT and volume swept reveals that the lithology model has a greater affect on recovery efficiency of a reservoir than the method of petrophysical property distribution (disregarding the grain-size model, which is discussed below). The continuous (LM-2) and discontinuous (LM-3) shale drapes on lateral-accretion surfaces within the point bar cause significant effects on BTT, volume swept at BTT, and sweep efficiency. The continuous shales act as both a vertical and lateral baffle to flow, causing an increased BTT. Because these baffles are continuous, no preferential paths of fluid flow are established; therefore the sweep efficiency is still reasonable. The discontinuous shales act mainly as vertical permeability baffles, and force updip-directed flow upward and downdip-directed flow downward (Hartkamp-Baker and Donselaar, 1993). This causes fluid to be directed towards the base of the point bar where there are no shale drapes, reducing the BTT as well as the volume swept. This lithologic distribution is representative of what is observed in most point-bar deposits, since shale drapes are not typically preserved over the entire lateral-accretion surface.

The petrophysical distributions based on grain size have a drastic affect on recovery efficiency. Regardless of the lithology model used to apply the permeability transform, resulting BTT and volume swept were similar. This is due to the fact that each model already accounts for changes in lithology, and the only difference between the models is the magnitude of the permeability baffle. The faster BTT and lower sweep efficiency predicted from these models is similar to production results from the subsurface.

In summary, based on these results, it is essential to include internal stratigraphic architecture within a point-bar sand body when generating geologic models that will be used for reservoir flow simulation. Without the inclusion of these features, BTT and volume swept are overestimated. This heterogeneity may be

included by constraining to simple sand/shale lithology models or by using a finer-scale measure of the spatial variability of petrophysical properties, such as grain-size or facies models.

CHAPTER FOUR

THREE-DIMENSIONAL POINT-BAR MODELING

MODELING OBJECTIVES

Two-dimensional geologic modeling and flow simulation can often be overly pessimistic in predicting reservoir behavior and performance (Li and White, 2003). The results of 2-D outcrop modeling in this study show that the internal architecture of a point bar does have a significant affect on reservoir compartmentalization, fluid storage, and flow. A 3-D model of a point bar was constructed using the same outcrop data in order to reassess the effect of lithologic and petrophysical distribution on fluid flow and storage. Li and White (2003) conducted a study on distributary channel point bars in the Ferron Formation using ground-penetrating radar data to assess the affect of internal shales on fluid flow. The authors concluded that the shale volume fraction of the model is the most significant factor affecting fluid flow compared to the variogram range (both parallel and perpendicular to paleoflow direction), but the effects are modest when shale volume is low. They state that heterogeneity in 3-D is commonly less than in 2-D.

Methods used to build the 3-D model were similar to those applied in 2-D modeling. The lithology modeling scenarios and petrophysical distributions were kept consistent so that direct comparisons could be made between the modeling results. Roxar's IRAP-RMS software was used to build the models, which are included in digital format on the attached CD-ROM and explained in Appendix F.

MODELING FRAMEWORK

Point-Bar Geometry

The younger point bar (M-1b) from the outcrop in Coal Canyon is the focus of 3-D modeling. The model framework consists of the top and base of the point bar with four internal lateral-accretion surfaces, and was constructed using several constraints and assumptions. For the general shape of the point bar, published data on modern and exhumed ancient point bars was used as a guide (Puigdefabregas, 1973; Jackson, 1976; Nanson, 1980; Edwards et al., 1983). In defining this shape, an assumption was made that the entire point bar was preserved, although the upstream portion of point bars are often destroyed during channel avulsion. The top and base of the point bar were constrained using the interpreted surfaces from the three outcrops obtained from lidar data (Figure 4.1). Meander amplitude was estimated to be approximately 300 m (980 ft) based on the extent of the sand body outcrop (i.e. sand body pinch-out) perpendicular to paleoflow. Meander wavelength and sinuosity were determined using the estimated values calculated from empirically derived equations, as described in Chapter Two. An intermediate value of 750 m (2,460 ft) was used as the maximum lateral extent of the point bar. The curvature of the point-bar shape was achieved by applying a sinuosity of 1.8, as determined from empirical estimates. Surface topography of the point bar was based on published, experimental data that predicts the maximum variation in topography and the thickest part of the point bar occurs at the bend apex (Willis, 1989). This assumes that bed topography is in equilibrium with water flow and bed-load transport (Bridge, 1992). The internal geometries present within the point bar were included in the 3-D model in a simplified form. Three of the main lateral-accretion surfaces observed in the northwest outcrop were contoured over the same area as the defined point bar. A fourth accretion surface was added outside of the

boundaries of the northwest outcrop. The geometry and character of the lateral-accretion surfaces were preserved from the outcrop, the dip of the surfaces is approximately 12 degrees and the surfaces are relatively flat to slightly concave downward.

Grid Construction

Contour maps defining the top and base of the point bar and the four internal accretion surfaces were gridded to define the modeling framework. The accretion surfaces were duplicated and the z-values on one surface were decreased by 10 cm (4 in) to create an upper bounding surface, in order to restrict the placement of shales to this interval during lithology modeling and subsequent petrophysical modeling. Using these ten surfaces, an XY regular modeling grid was generated with 100 rows by 100 columns. Nine subgrids were generated with varying cell thicknesses (Figure 4.2). Cell dimensions are 7.8 m (25.6 ft) by 4.1 m (13.5 ft) aerially and have variable cell thickness. Those subgrids that define a lateral-accretion surface where shale lithologies may be present were populated with cells 0.05 m (2 in) thick. All other subgrids used a cell thickness of 0.5 m (20 in). All cells within the model were top-truncated. The resulting model consists of a total of 810,000 cells

LITHOLOGY MODELING

Methods

Three deterministic lithology models were created within the 3-D framework, similar to those created for the 2-D outcrop models. The lithologies modeled include sand and shale. Instead of using the interpolation algorithm as applied in 2-D modeling, other methods were used to populate the model. For the first two lithology

models, discrete values were assigned to cells by filtering based on subgrids. This was possible because separate subgrids were created for the lateral-accretion surfaces, which were not included in 2-D modeling. For the third lithology model, sand/shale aerial trend maps were imported from Petra and used to assign lithology within the model such that shales are only present on the topographically higher portions of the accretion surfaces with sand-on-sand contacts present in the topographic lows.

Results

The lithology modeling scenarios represent three levels of internal lithologic heterogeneity (Figures 4.3 and 4.4). Lithology Model 1 (LM-1) is composed of 100% sand, with no internal lithologic heterogeneities. Lithology Model 2 (LM-2) has continuous shale drapes along the four defined lateral-accretion surfaces. By volume, this model contains 99.3% sand and 0.7% shale. Lithology Model 3 (LM-3) has discontinuous shale drapes along the lateral-accretion surfaces, with the shales confined to the topographically higher portions of the surface. The shale volume in this model is 0.3%, with 99.7% sand. LM-1 exhibits the lowest spatial variability, with LM-2 having the highest.

Discussion

LM-1 represents the homogeneous point-bar model in which there are no internal lithologic variations. LM-2 treats the entire lateral-accretion surface as a permeability baffle, while LM-3 has only the topographically higher portions of the surface as a baffle. LM-1 is an optimistic scenario in terms of reservoir potential, while LM-2 may be overly pessimistic, since shales are not often continuous across accretion surfaces. LM-3 represents the most probable scenario based on the

outcrops within Coal Canyon, as well as other outcrop studies, modern analogs, and the principles of hydrodynamics and sediment deposition. It should be noted that, for simplicity, only four accretion surfaces were included in the lithology model, which underestimates the actual internal lithologic heterogeneity of this outcrop point bar. In reality, a point-bar reservoir would include a more complex stratigraphic architecture, leading to a higher lithologic variability. Shale volume is also grossly underestimated in these lithology models. Therefore, these models should be considered to include a minimum amount of internal lithologic heterogeneity.

GRAIN-SIZE MODELING

Methods

Grain-size modeling is a useful method to represent the internal heterogeneity within a point bar, similar to the application of facies modeling. Sedimentologic data from 13 sections measured on the three outcrops (Appendix A) were used to create grain-size logs, tied to their approximate location within the 3-D model. The median grain size corresponding to each size classification (e.g. medium sand = 0.297 mm [0.01 in]) was recorded as the grain-size value. An additional forty grain-size logs were created based on the vertical changes seen in outcrop and placed in specific locations throughout the model. These grain-size logs assisted the interpolation algorithm used to populate the model with grain-size values to produce the desired grain-size distribution. Each subgrid within the model was interpolated separately. A radius of influence of 700 m (2,300 ft) was used in the x- and y-directions, and 0.5 m (1.6 ft) in the z-direction. No influence orientation was used. This algorithm created a continuous 3-D grain-size parameter within the modeling area.

Results

A single grain-size model of the 3-D point bar was generated (Figure 4.5). The average grain size in the model is 0.173 mm (0.007 in) or fine sand, with a minimum of 0.033 mm (0.001 in) and a maximum of 0.297 mm (0.01 in), silt and lower-medium sand, respectively. These grain-size ranges are consistent with observations made from the outcrop. The visually-estimated grain-size correlation length perpendicular to paleoflow is 50 to 100 m (160 to 330 ft), 100 to 200 m (330 to 660 ft) parallel to paleoflow, and less than 0.5 m (1.6 ft) in the vertical direction. These ranges are larger than those observed in 2-D modeling of the northwest outcrop. In general, a fining-upward grain-size trend was observed over the entire point bar.

Discussion

The point-bar grain-size model is a simplification of observed grain-size trends in modern and ancient point-bar deposits. In process-based simulated point-bar models, the majority of sections fine upward, due to the small amount of point-bar migration by translation needed to erode coarsening-upward deposits that are typically present on the upstream portion of the bar (Willis, 1989). A fining-upward trend is observed at all locations within the model, both on the scale of individual accretion units and the entire point-bar deposit. Grain size changes within the point bar are related to general facies changes observed in outcrop. In reality, coarsening-upward deposits and massive sand may be present within a point bar. Smaller scales of grain-size variation (i.e. laminae scale, bed, or bed set) are also present within point bars, but are not addressed in this study.

PETROPHYSICAL MODELING

Modeling Scenarios

Three methods of distributing petrophysical properties were used to generate porosity and permeability models of the point bar. Both deterministic and stochastic methods were applied, including a uniform distribution (deterministic), a conditional simulation distribution (stochastic), and a distribution based on grain size (deterministic). The uniform distribution scenario assigns a single value of porosity and permeability to a certain lithology. Based on the results of 2-D outcrop modeling, significant differences were not observed between the two stochastic modeling methods, conditional simulation and conditional simulation with a linear trend. Therefore only conditional simulation was used in 3-D petrophysical modeling. The grain-size model was directly transformed to porosity and permeability based on several assumptions. The permeability transform used in 2-D modeling was also applied in 3-D modeling for comparison purposes. Examination of these three scenarios will provide insight to the effect of the distribution of petrophysical properties on fluid flow and storage in a 3-D volume.

Porosity Modeling

Methods

The methods used to distribute porosity within the 3-D point-bar model were the same as those used in 2-D outcrop modeling and are described in detail in the previous chapter (Chapter Three). The uniformly distributed models were built using the subgrid and facies filter to assign a single value of porosity to both sand and shale. Conditional simulation was conducted using an FFT transform based on an input histogram and variogram. These inputs were derived from data collected from

the three outcrops in Coal Canyon. Grain size was transformed to porosity using a simple transform which correlated maximum porosity with maximum grain size.

Results

Seven porosity models were generated for the 3-D point-bar model. The distributions are shown together in Figure 4.6 for comparison. Statistical data for all porosity models is summarized in Appendix G.1.

The porosity models with a uniform distribution are U-1, U-2, and U-3 (Figures 4.7 and 4.8). Model U-1 has a single value of porosity, equal to 9.0%. This model was constrained by LM-1, the homogeneous point-bar scenario. Model U-2 has an average porosity of 8.4%, with a maximum and minimum porosity of 9.0% and 1.0%, respectively. This decreased average porosity is due to the presence of continuous shale drapes on the four lateral-accretion surfaces, as defined in LM-2. Model U-3 has an average porosity of 8.7% and a 1.0% minimum and 9.0% maximum porosity. In this model, shale porosities are confined to the upper portion of the lateral-accretion surfaces, conditioned using LM-3. These uniformly distributed models represent the simplest and most continuous spatial distribution of porosity compared to the other distribution scenarios that were tested.

Three porosity models were stochastically generated using conditional simulation, including CS-1, CS-2, and CS-3 (Figures 4.9 and 4.10). Spatial continuity of porosity in these models is controlled by the input variograms. Model CS-1, conditioned to LM-1, has an average porosity of 9.0%, with a minimum porosity of 6.0% and a maximum porosity of 12.0%. The average porosity of model CS-2 is 8.4%, with 1.0% and 12.0% as the minimum and maximum porosities and was conditioned using LM-2. Model CS-3, conditioned using LM-3, has an average porosity of 8.7%, with 1.0% and 12.0% as the minimum and maximum porosities.

These models, in comparison with the other two scenarios, have the most random and discontinuous distribution of porosity.

The 3-D point-bar grain-size model was transformed to create a single porosity model based on grain size (Figure 4.11). The average porosity in this model is 6.8%, with a minimum of 1.0% and a maximum of 12.0%.

Overall, the average porosities of the models with a uniform and conditionally simulated distribution are similar. Average porosity in the model derived from the grain-size distribution is 1.0 to 2.0% lower. Aside from the uniformly distributed models, the grain-size model exhibits the highest spatial continuity. LM-1 has the highest porosity and lateral continuity among the lithology models, with LM-2 having the lowest porosity and lateral continuity.

Discussion

Pore volume within a point-bar reservoir is determined by the porosity distribution. Average porosities are highest in LM-1, due to the lack of low pore volume shales. LM-3 and LM-2 have increasingly higher amounts of shale and result in lower overall porosity. The uniform and conditionally simulated models have approximately the same average porosities because the porosity of 9.0%, chosen for the uniform models, is also the average porosity of the input histogram which is honored in the conditionally simulated models. The lower porosities observed in the grain-size models suggest that the other distribution methods overestimate porosity compared to observed outcrop trends. This is based on the assumption that the full range of porosities (6 to 12%) is present within the point bar.

Permeability Modeling

Methods

To maintain consistency between the 2-D and 3-D models, the same transform was used to calculate permeability from the porosity models. This transform uses a shifted porosity/permeability relationship from analog data in a North Sea fluvial reservoir (see Permeability Modeling section in Chapter Three). A separate transform was used for sand and shale lithologies by applying a lithology filter prior to the transform.

Results

Nine permeability models were produced using the previously generated porosity models. The three distribution methods are shown together in Figure 4.12 for comparison. Statistical data for the permeability models is summarized in Appendix G.2.

Permeability models with a uniform distribution, U-1, U-2, and U-3, were generated using their correlative porosity models (Figures 4.13 and 4.14). Within the point bar, model U-1 has a single permeability value of 192 md. Model U-2 has an average permeability of 178.5 md, with minimum and maximum permeability values of 0.06 md and 192 md, respectively. Model U-3 has an average permeability of 185.7 md, with 0.06 md and 192 md as the minimum and maximum permeabilities, respectively.

Three permeability models, CS-1, CS-2, and CS-3, were created using the conditionally simulated porosity models (Figures 4.15 and 4.16). Model CS-1 has a range of permeabilities from 70 to 505 md, with an average of 284.2 md. Model CS-2 permeabilities ranged from 0.07 to 505 md, averaging 264.9 md. Model CS-3 has

an average permeability of 275.5 md with a minimum and maximum permeability of 0.07 md and 505 md, respectively.

Using the single porosity model, three lithology models, and two transform equations (Chapter Three), three permeability models, GS-1, GS-2, and GS-3, were generated based on grain size (Figures 4.17 and 4.18). Model GS-1 has an average permeability of 130.4 md, with minimum and maximum values of 14.9 and 503 md, respectively. Model GS-2 has a range of permeabilities between 0.07 and 503 md, with an average of 129.4 md. Model GS-3 has an average permeability of 129.9 md, with a minimum of 0.07 md and a maximum of 503 md.

The permeability models exhibit the same trends as those observed from porosity modeling, due to the use of a direct transformation. The average permeabilities for the uniform and conditionally simulated models are higher than for the grain-size models. The uniform models exhibit the highest spatial continuity, followed by the grain-size models and the conditionally simulated models. Permeability models constrained to LM-1 have the highest permeabilities, while those constrained to LM-2 have the lowest permeabilities.

Discussion

The permeability distribution within a point bar will control preferential fluid-flow paths through the reservoir and have an impact on breakthrough times and recovery efficiencies. By simply comparing permeability patterns within the model, it is possible to predict fluid behavior by identifying connected zones of enhanced permeability.

The uniformly distributed models have only a single value of permeability assigned to sand, which results in all potential fluid paths having an equal probability of occurring. The presence of shale baffles within the uniformly distributed models

will act as lateral flow baffles in the case of LM-2 and vertical baffles for LM-3. The conditionally simulated models have areas of high permeability distributed laterally and vertically throughout the model. These areas create a disconnected network of preferential fluid paths, leading to tortuous permeability paths within the reservoir. Interaction of the shale baffles within these models is difficult to predict because of the random spatial distribution of high permeability zones, but they will likely have similar affects as those seen with the uniformly distributed models. The grain-size models have a continuous and connected high permeability path at the base of the reservoir, corresponding to the largest grain sizes and highest porosities. Fluid flow will likely remain concentrated in this high permeability zone. The lateral permeability baffles in LM-2 will inhibit flow across these surfaces, and the vertical baffles in LM-3 will be largely avoided because the fluid will remain at the base of the reservoir.

VOLUMETRICS

Methods

Fluid storage in reservoirs is primarily controlled by the matrix properties of the rock. The distribution of the bulk sand volume is a calculation of all sand within the reservoir and it is useful to assess connectivity and compartmentalization. Pore volume is the space in a rock that fluids may occupy. Bulk volume and pore volume were calculated on the resulting three lithology models and seven porosity models in order to quantify the storage potential of each scenario.

Results

Calculated bulk-sand volumes from the three lithology models are summarized in Table 4.1. LM-1 resulted in the highest sand volume, 1.06×10^6 m^3

(3.73×10^7 ft^3), within a single reservoir compartment. LM-2 had the lowest sand volume, 9.12×10^5 m^3 ($3.22 * 10^7$ ft^3), which was divided into four reservoir compartments. This volume is 14% less than that of LM-1. LM-3 had an intermediate sand volume of 1.05×10^6 m^3 ($3.72 * 10^7$ ft^3), only 1.0% less than the volume of LM-1, and resides in a single compartment.

Calculated pore volumes include shale pore volume, although the affect is negligible. Results from the pore volume calculations are presented in Table 4.2. Pore volume for the uniformly distributed models was the highest of the three distribution scenarios. The single grain-size model had the lowest pore volume. Among the lithology models used to constrain petrophysical distribution, LM-1 resulted in the highest pore volumes while LM-2 had the lowest.

ANOVA was conducted to interpret the significance of the pore volume results between the various distribution methods (Appendix H.1 to H.2). When testing the petrophysical distributions, the null hypothesis was rejected (F-ratio [4397] > F-critical [5.143]), indicating a significant difference between the average pore volumes for each distribution method. A low p-value (0.000) suggests that this difference is highly significant and not due to randomness. Comparison of the three lithology models used to condition the uniform and conditionally simulated porosity models (only one porosity model based on grain size was generated) resulted in accepting the null hypothesis (F-ratio [0.001] < F-critical [5.143]), suggesting that pore volume is not significantly different between the lithology models.

Discussion

The difference in bulk volume between LM-1 and LM-3 is small as a result of the low volume of shale and the lack of continuous barriers that would cause compartmentalization.

Pore volume estimations are used to calculate the fluid in place within a reservoir, and are a major factor in determining the economic viability of a reservoir. Assuming that shale does not account for a substantial bulk volume of the reservoir, these results show that including shale volume does not have a significant impact on pore volume calculations. The spatial distribution of porosity within the sand lithology does appear to impact pore volume estimates, and should be accounted for when calculating field reserves. Determining which porosity distribution to use is dependent on the amount of data available for a particular reservoir. Based on the results of this study, using a uniform or stochastically generated distribution may result in overestimating pore volume if grain size and porosity are directly related.

STREAMLINE SIMULATION

Methods

Simple streamline simulations were conducted using the resulting porosity and permeability models of the 3-D point bar. The same input rock and fluid parameters used in 2-D simulation were also applied to 3-D simulation, and are presented in Table 3.6.

Two well patterns were used to compare the relative affect of the orientation of fluid flow with respect to the architectural framework. Well Pattern 1 was oriented such that injected fluid would travel parallel to paleoflow. Injector 1 is located on the east side of the point bar and Producer 1 is on the west side. Well Pattern 2 was oriented such that the injected fluid would travel perpendicular to paleoflow. Injector 2 is located on the south side of the model and Producer 2 is on the north side. This well pattern is comparable to the arrangement used in 2-D outcrop modeling.

Results

The simulation results address breakthrough time (BTT), volume swept at BTT, and sweep efficiency, which are presented for both Well Pattern 1 and Well Pattern 2 in Tables 4.3 and 4.4. In addition to these numerical data, more qualitative assessments are made by visually comparing the appearance of the fluid fronts (Figures 4.19, 4.20, 4.21, 4.22, 4.23, and 4.24).

BTTs for Well Pattern 1 were significantly longer than those for Well Pattern 2. In Well Pattern 1, BTT was the longest for the uniformly distributed models and the models constrained to LM-1 (Figure 4.25). For Well Pattern 2, the uniformly distributed models also produced the longest BTT, but LM-2 had the longest BTT when comparing lithology models (Figure 4.26). BTT was the shortest for the models based on the grain-size distribution and constrained to LM-3 in both well sets.

ANOVA for the BTT results was conducted to evaluate whether the differences observed between lithology models and petrophysical distribution are statistically significant (Appendix H.3 to H.6). Comparison of BTT based on the lithology model for Well Pattern 1 results in acceptance of the null hypothesis (F-ratio [0.079] < F-critical [5.143]), suggesting that the lithology model used does not have a large impact on BTT. For the three petrophysical distributions with Well Pattern 1, the rejection of the null hypothesis (F-ratio [96.54] > F-critical [5.143]) and the low p-value (0.000) indicates that there is a significant difference between the BTT for the four petrophysical distributions that is not due to a random event. For Well Pattern 2, when comparing the lithology models the null hypothesis was rejected (F-ratio [8.454] > F-critical [5.143]) and the low p-value (0.018) indicates that the differences observed are not due to random events. Comparison of the petrophysical distributions results in accepting the null hypothesis (F-ratio [0.8974] < F-critical

[5.143]), suggesting that in this orientation, the petrophysical distribution does not have a significant affect on BTT. The results of the ANOVA analysis for Well Pattern 2 are consistent with those observed in 2-D modeling.

Volume swept and sweep efficiency are directly proportional to the observed BTT. As a result, sweep efficiencies for Well Pattern 1 are greater than those for Well Pattern 2. For Well Pattern 1, the uniformly distributed models and the models constrained to LM-1 have the greatest volume swept and the highest sweep efficiencies (Figure 4.27). For Well Pattern 2, the uniformly distributed models and the models constrained to LM-2 have the greatest volume swept and highest sweep efficiencies (Figure 4.28). The grain-size models yielded the lowest sweep efficiencies for both Well Pattern 1 and 2.

Using the volume swept at BTT, ANOVA was conducted to evaluate the significance of the results (Appendix H.7 to H.10). Comparison between lithology models for Well Pattern 1 results in accepting the null hypothesis (F-ratio [0.096] < F-critical [5.143]), revealing that the volumes swept are not statistically different between the three scenarios. The same analysis for the petrophysical distributions for Well Pattern 1 results in rejecting the null hypothesis (F-ratio [81.13] > F-critical [5.143]) with a low p-value (0.000), which suggests that the method of distribution significantly affects the sweep efficiency. For Well Pattern 2, the analysis of variance when comparing the lithology models causes rejection of the null hypothesis (F-ratio [9.487] > F-critical [5.143]), and low p-value (0.014) suggests that the variance is significant. Comparison of the petrophysical distributions leads to accepting the null hypothesis (F-ratio [0.7835] < F-critical [5.143]), indicating that the distribution method does not have a significant affect on volume swept at BTT in this orientation.

Discussion

Streamline simulation results suggest that lithologic and petrophysical heterogeneity do significantly affect fluid flow within a 3-D point-bar reservoir. Additionally, the results are influenced by the spatial arrangement of the injection and production wells with respect to the orientation of the point bar.

In the case of the injected fluid traveling parallel to the paleoflow direction, as with Well Pattern 1, the influence of internal lithologic changes is minimal. Conversely, the lithologic distribution acts to enhance lateral flow. The shale baffles present in LM-2 act to segregate flow into separate compartments, which causes a decrease in BTT. The barriers present on the topographic highs of the accretion surfaces in LM-3 do not force flow to the base of the reservoir, resulting in an increased BTT. Fluid flow in this orientation is more sensitive to the distribution of permeability, which controls the tortuosity of the flow path. The conditional simulation created the most tortuous path for fluid flow, leading to increased BTT, as well as higher sweep efficiency, since the fluid had to search for a preferential path. The grain-size distribution provided the most direct, high permeability pathway, such that fluid did not seek out other areas of the reservoir, resulting in a decreased BTT and sweep efficiency.

In the case of injected fluid traveling perpendicular to the paleoflow direction, as with Well Pattern 2, internal lithologic changes significantly affect simulation results. Shale drapes in this orientation act as lateral permeability baffles in the case of LM-2, forcing the fluid to slowly travel across these continuous surfaces, resulting in a relatively higher BTT compared to LM-1. The discontinuous shales in LM-3 act more as vertical permeability baffles, forcing fluid downward to the base of the point bar, leading to a relatively lower BTT compared to LM-1. Sweep efficiency is also decreased in this case because the fluid is focused in one area and does not

infiltrate the upper portions of the reservoir. The lithologic distribution is the dominant factor in controlling BTT and sweep efficiency in this orientation.

Because Well Pattern 1 is oriented parallel to the long axis of the point bar (i.e. meander wavelength), BTT, volume swept, and sweep efficiency are higher than Well Pattern 2 since the fluid must travel more than three times the distance compared to Well Pattern 2 (most direct path for Well Pattern 1 is 728 m [2,390 ft] versus 220 m [720 ft] for Well Pattern 2). By accounting for this distance, it is possible to directly compare the simulation results based on the orientation of fluid flow in reference to the paleoflow direction of the point bar (Table 4.5). If this factor were removed, BTT, volume swept at BTT, and sweep efficiency are higher in LM-1 and LM-3 when fluid is swept parallel to paleoflow (Well Pattern 1) versus perpendicular to paleoflow (Well Pattern 2). Yet, for LM-2, the opposite is true, and sweep efficiency is maximized when fluid flow is oriented perpendicular to paleoflow. These results suggest that when producing a reservoir with a lithologic distribution similar to that of LM-3 (which is the most realistic of the three lithology models); it is most favorable to orient the wells such that flow is directed parallel to paleoflow.

CHAPTER FIVE

CONCLUSIONS AND RECOMMENDATIONS

CONCLUSIONS

Detailed sedimentologic and stratigraphic measurements of outcrop exposures, acquisition and analysis of high-resolution lidar data, and numerical modeling studies were integrated to quantify the effects of stratigraphic and petrophysical heterogeneity on fluid flow and potential storage within fluvial point-bars. The results of this study suggest that the internal heterogeneities present within point-bar deposits can have a significant impact on predicting reservoir behavior and performance and hence, should be included in reservoir modeling.

Sedimentology and Stratigraphy

Sedimentologic data were collected from three outcrops in Coal Canyon and were used to identify and interpret key facies, including trough cross-bedded sandstone, current-rippled sandstone, and conglomeratic mud-chip sandstone (all of which are potential reservoir facies). Grain size and sedimentary structures were used to quantitatively approximate paleoflow conditions. Water depths are interpreted to have ranged from 1.2 to 3 m (3.9 to 9.8 ft) and flow velocities of 30 to 80 cm/sec (12 to 31 inch/sec). Vertical facies associations reveal a repeated fining-upward trend in both grain size and scale of sedimentary structures.

Stratigraphic analysis of the outcrops in Coal Canyon revealed a systematic and ordered nature of bedforms at multiple scales, including macro-, meso-, and microforms. The main sand body present in the outcrop consists of two macroforms, separated by an internal erosion surface. Within each macroform are high-angle

bounding surfaces, creating potential reservoir baffles due to the presence of shale drapes.

The sedimentologic and stratigraphic analyses provide evidence for interpreting the depositional environment for various architectural elements present in the outcrop. An amalgamated point-bar sand body was interpreted based on the: 1) the internal arrangement of facies in fining-upwards cycles on the scale of both individual accretion units and the entire sand body, 2) the presence of an overall lens-shaped geometry, and 3) high-angle surfaces (lateral-accretion surfaces) representing depositional time lines. This interpretation is consistent with previous interpretations of these specific deposits by Cole et al. (2002).

Paleochannel reconstruction of the point bar was conducted to estimate various morphologic characteristics. These parameters are directly related to the shape and lateral extent of the sand body and are used to reconstruct the 3-D geometry of the point bar for subsequent modeling. Applying several empirically derived methods, it was estimated that the river system responsible for depositing the point bar had a bankfull channel width and depth of 44.4 m (146 ft) and 4.9 m (16 ft), respectively, a sinuosity of 1.8, a mean annual discharge of 46.8 cms (1653 cfs), and a meander wavelength of approximately 750 m (2,460 ft).

2-D Outcrop Modeling

Two-dimensional models of lithology, grain size, porosity, and permeability, based on the northwest outcrop in Coal Canyon, were constructed using both deterministic and stochastic techniques. Lidar data assisted with interpreting the stratigraphic framework and provided a method for constraining the models to the outcrop. Streamline simulation and volumetric calculations were used to quantify the

effect of heterogeneity associated with different lithologic and petrophysical scenarios.

Drainable volume calculations suggest that lithologic variations within a point bar, specifically lateral-accretion surfaces, cause compartmentalization within the reservoir. Based on the stratigraphic complexity of the sand body and the continuity of shale-draped accretion surfaces, optimized placement of vertical wells is variable. As a result, the placement of a horizontal well will maximize the number of compartments drained regardless of these two factors. Pore-volume estimates suggest that the method of spatial distribution of porosity is a significant controlling factor, where as the lithologic distribution is minimal.

Streamline simulation results indicate that the lithologic distribution observed in outcrop (LM-3) forces fluid to the base of the reservoir due to the presence of vertical permeability baffles, causing a decrease in BTT and sweep efficiency. The method of distributing petrophysical properties did not have a significant influence on the simulation results, except in the case of the grain-size models, which resulted in an even lower BTT and sweep efficiency.

3-D Point-Bar Modeling

Because 2-D models have been shown to be overly pessimistic with regard to fluid flow and volume estimates, a 3-D theoretical point-bar model, based on outcrop data collected in Coal Canyon, was constructed to assess the effect of internal heterogeneities. This model represents a minimum amount of potential stratigraphic heterogeneity, and shale volume is largely underestimated.

Drainable-volume calculations of a point-bar reservoir indicate that lithologic variability does not have a significant impact due to the low bulk volume of shales present in the lithology models. These variations, however, can cause

compartmentalization within a reservoir where shales are laterally continuous. The spatial distribution of porosity within a reservoir has a considerable impact on the pore volume, and is an important factor to consider when calculating reserves-in-place.

Results of streamline simulation indicate that the effect of internal heterogeneities on fluid flow varies according to the arrangement of wells with respect to the point-bar orientation. When fluid flow is oriented perpendicular to the paleoflow direction, the flow is forced to the base of the point bar due to shale baffles on the topographic highs of lateral-accretion surfaces. This results in a relatively lower BTT and sweep efficiency compared to the homogeneous case. Alternatively, when fluid flow is oriented parallel to the paleoflow direction, the shale baffles act to promote lateral and vertical flow, resulting in a higher relative BTT and sweep efficiency, compared to the homogeneous model. Therefore, it appears to be more effective to drain a point-bar reservoir by forcing fluid flow parallel to the point-bar paleoflow orientation.

2-D and 3-D Modeling Comparison

The results of both 2-D and 3-D modeling indicate that the internal lithologic and petrophysical heterogeneities in point bars have a significant affect on fluid flow and storage. Although the effect on the resulting parameters is more dramatic in 2-D, it may not be adequate to use a simple, homogeneous model with no internal heterogeneity in a 3-D reservoir model. ANOVA analyses on both the 2-D and 3-D models reveal that the differences observed in drainable volume, pore volume, BTT, volume drained at BTT, and sweep efficiency between the lithologic and petrophysical distributions are, in most cases, statistically significant.

RECOMMENDATIONS

The reservoir modeling discipline is rapidly changing and expanding to incorporate new techniques and approaches. Geologic models of outcrops, in particular, provide an opportunity to observe detailed stratigraphic architecture that may be captured to improve subsurface geologic modeling. Based on the results of this study, it is recommended that the following areas be addressed in future work:

1. Generate a detailed facies model across the outcrop modeling area to compare to the grain-size models.
2. Collect samples from the outcrop and perform porosity and permeability measurements to establish a relationship between grain size, sedimentary structures, and petrophysical properties.
3. Apply techniques such as ground-penetrating radar in order to more accurately represent the 3-D geometry and arrangement of internal stratigraphic units.
4. Investigate different variogram ranges and model types for the stochastically-generated models, such as incorporating a nugget effect to account for small-scale variability of petrophysical properties.
5. Examine upscaling techniques that will preserve the level of detail included in the models without compromising computing limitations.
6. Build a more realistic 3-D point-bar model that includes a greater number of internal bounding surfaces with a complex spatial arrangement and a higher overall shale volume.
7. Investigate the drainage patterns and sweep efficiencies of horizontal wells in order to assess the advantages and disadvantages of horizontal drilling compared to vertical drilling.

8. Run conventional fluid-flow simulations to compare with streamline simulation results.

REFERENCES

Allen, J. R., 1963, The classification of cross-stratified units with notes on their origin: Sedimentology, v. 2, p. 93 - 114.

Allen, J. R., 1965, The sedimentation and palaeogeography of the Old Red Sandstone of Anglesey, North Wales: Proceedings of the Yorkshire Geological Society, v. 35, p. 139 - 185.

Allen, J. R., 1970, Studies in fluviatile sedimentation: a comparison of fining-upward cyclothems, with special reference to coarse-member composition and interpretation: Journal of Sedimentary Petrology, v. 40, p. 298 - 323.

Allen, J. R., 1978, Studies in fluviatile sedimentation: an exploratory quantitative model for the architecture of avulsion-controlled alluvial suites: Sedimentary Geology, v. 21, p. 129 - 147.

Allen, J. R., 1983, Studies in fluviatile sedimentation; bars, bar-complexes, and sandstone sheets (low sinuosity braided streams) in the Brownstones (L. Devonian), Welsh Borders: Sedimentary Geology, v. 33, no. 4, pg. 237 - 293.

Allen, J. R., 1984, Sedimentary structures: their character and physical basis: New York, Elsevier Publishing, Developments in Sedimentology, v. 30, 663 p.

Anderton, R., 1985, Clastic facies models and facies analysis, in P. J. Brenchley and B. P. J. Willams, eds., Sedimentology; recent developments and applied aspects, Oxford, Blackwell Science Publishing, p. 31 - 46.

Ashley, G. M., J. B. Southard, and J. C. Boothroyd, 1982, Deposition of climbing-ripple beds – a flume simulation: Sedimentology, v. 29, p. 67 - 79.

Bellian, J., D. Jennette, C. Kerans, J. Gibeaut, J. Andrews, B. Ysseldyk, and D. Larue, 2002, Three-dimensional digital outcrop data collection and analysis using eye-safe laser (lidar) technology (abs.): AAPG 2002 Meeting, Houston, Texas, March 10 - 13, 2002.

Beard, D. C. and P. K. Weyl, 1973, Influence of texture on porosity and permeability of unconsolidated sand: AAPG Bulletin, v. 57, no. 2, p. 349 - 369.

Blakey, R. C., 2004, Cretaceous paleogeography of the southwestern US, <http://jan.ucc.nau.edu/~rcb7/crepaleo.html> Accessed March 12, 2004.

Box, G. E. P., W. G. Hunter, and J. S. Hunter, 1978, Statistics for experimenters: an introduction to design, data analysis, and model building: New York, John Wiley and Sons, 653 p.

Bridge, J. S., 1992, A revised model for water flow, sediment transport, bed topography, and grain size sorting in natural river bends: Water Resources Research, v. 28, no. 4, p. 999 - 1013.

Bridge, J. S. and M. R. Leeder, 1979, A simulation model of alluvial stratigraphy: Sedimentology, v. 26, p. 617 - 644.

Bridge, J. S. and S. D. Mackey, 1993, A theoretical study of fluvial sandstone body dimensions, in S. S. Flint and I. D. Bryant, eds., The geological modelling of hydrocarbon reservoirs and outcrop analogs: Special Publication 15 of the International Association of Sedimentologists, p. 213 - 236.

Bridge, J. S. and R. S. Tye, 2000, Interpreting the dimensions of ancient fluvial channel bars, channels, and channel belts from wireline-logs and cores: AAPG Bulletin, v. 84, no. 8, p. 1205 - 1228.

Caracuel, J. E., J. Cardenal, G. J. Delgado, and L. S. Garcia, 2000, A simple photogrammetric method to improve quantitative image analysis in geoscience research: Journal of Sedimentary Research, v. 70, no. 6, p. 1337 - 1340.

Carlston, C. W., 1965, The relation of free meander geometry to stream discharge and its geomorphic implications: American Journal of Science, v. 263, p. 864 - 885.

Cashion, W. B., 1973, Geologic and structural map of the Grand Junction Quadrangle, Colorado and Utah: United States Geological Survey Map I-736, scale 1:250,000, 1 sheet.

Cole, R., S. Cumella, M. Boyles, and G. Gustason, 2002, Stratigraphic architecture and reservoir characterization of the Mesaverde Group, Northwest Colorado: Field Trip #2 in conjunction with the 2002 Rocky Mountain Sectional Meeting of the AAPG, Laramie, WY, Sept. 6 - 8, 2002, 80 p.

Cole, R. and S. Cumella, 2003, Stratigraphic architecture and reservoir characteristics of the Mesaverde Group, southern Piceance Basin, Colorado, in K. M. Peterson, T. M. Olsen, and D. S. Anderson, eds., Piceance Basin 2003 guidebook: Rocky Mountain Association of Geologists, p. 385 - 442.

Collinson, J. D., 1978, Vertical sequence and sand body shape in alluvial sequences, in A. D. Miall, ed., Fluvial sedimentology: Canadian Society of Petroleum Geologists Memoir 5, p. 577 - 586.

Collinson, J. D. and D. B. Thompson, 1989, Sedimentary structures: London, Unwin Hyman, 207 p.

Cumella, S. P. and D. B. Ostby, 2003, Geology of the basin-centered gas accumulation, Piceance Basin, Colorado, in K. M. Peterson, T. M. Olsen, and D. S. Anderson, eds., Piceance Basin 2003 guidebook: Rocky Mountain Association of Geologists, p. 171 - 193.

Dalrymple, M., 2001, Fluvial reservoir architecture in the Statfjord Formation (northern North Sea) augmented by outcrop analogue statistics: Petroleum Geoscience, v. 7, p. 115 - 122.

Deutsch, C. V., 2002, Geostatistical reservoir modeling: Oxford, Oxford University Press, 376 p.

Dury, G. H., 1965, Theoretical implications of underfit streams: United States Geological Survey Prof. Paper 452-C, 43 p.

Edwards, M. B., K. A. Erikkson, and R. S. Kier, 1983, Paleochannel geometry and flow patterns determined from exhumed point bars in north-central Texas: Journal of Sedimentary Petrology, v. 53, no. 4, p. 1261 - 1270.

Eschard, R., P. Lemouzy, C. Bacciana, G. Desaubliaux, J. Parpant, and B. Smart, 1998, Combining sequence stratigraphy, geostatistical simulations, and production data for modeling a fluvial reservoir in the Chaunoy Field (Triassic, France): AAPG Bulletin, v. 82, no. 4, p. 545 - 568.

Ethridge, F. G. and S. A. Schumm, 1977, Reconstructing paleochannel morphologic and flow characteristics: methodology, limitations, and assessment, in A. D. Miall, ed., Fluvial sedimentology: Canadian Society of Petroleum Geologists Memoir 5, p. 703 - 722.

Friend, P. F., 1983, Towards a field classification of alluvial architecture or sequence, in J. D. Collinson and J. Lewin, eds., Modern and ancient fluvial systems: Special Publication of the International Association of Sedimentologists, no. 6, p. 345 - 354.

Gringarten, E. and C. V. Deutsch, 2001, Teacher's aide variogram interpretation and modeling: Mathematical Geology, v. 33, no.4, p. 507 - 534.

Grout, M. A. and E. R. Verbeek, 1992, Fracture history of the Divide Creek and Wolf Creek anticlines and its relation to Laramide basin-margin tectonism, southern Piceance Basin, northwestern Colorado: United States Geological Survey Bulletin 1787-Z, 32 p.

Hack, J. T., 1957, Studies of longitudinal stream profiles in Virginia and Maryland: United States Geological Survey Prof. Paper 294-B, p. 45 - 97.

Haldorsen, H. H. and L. W. Lake, 1984, A new approach to shale management in field-scale models: Society of Petroleum Engineers Journal, August 1984, p. 447 - 457.

Harms, J. C., D. B. MacKenzie, and D. G. McCubbin, 1962, Stratification of modern sands of the Red River, Louisiana: Journal of Geology, v. 71, p. 566 - 579.

Hartkamp-Bakker, C. A., and M. E. Donselaar, 1993, Permeability patterns in point bar deposits: Tertiary Loranca Basin, central Spain, in S. S. Flint and I. D. Bryant, eds., The geological modelling of hydrocarbon reservoirs and outcrop analogs: Special Publication 15 of the International Association of Sedimentologists, p. 157 - 168.

Hettinger, R. D. and M. A. Kirschbaum, 2002, Stratigraphy of the Upper Cretaceous Mancos shale (upper part) and Mesaverde Group in the southern part of the

Uinta and Piceance Basins, Utah and Colorado: United States Geological Survey Investigations Series I-2764, 21 p.

Hirst, J. P. P., C. R. Blackstock, and S. Tyson, 1993, Stochastic modeling of fluvial sandstone bodies, in S. S. Flint and I. D. Bryant, eds., The geological modelling of hydrocarbon reservoirs and outcrop analogs: Special Publication 15 of the International Association of Sedimentologists, p. 237 - 252.

Hoak, T. E. and A. L. Klawitter, 1997, Prediction of fractured reservoir production trends and compartmentalization using an integrated analysis of basement structures in the Piceance Basin, western Colorado, in T. E. Hoak, A. L. Klawitter, and P. K. Blomquist, eds., Fractured reservoirs: characterization and modeling: Rocky Mountain Association of Geologists Guidebook, p. 67 - 102.

Jackson, R. G., 1975, Hierarchical attributes and a unifying model of bed forms composed of cohesionless material and produced by shearing flow: Geological Society of America Bulletin, v. 86, p. 1523 - 1533.

Jackson, R. G., 1976, Depositional model of point bars in the Lower Wabash River: Journal of Sedimentary Petrology, v. 46, no. 3, p. 579 - 594.

Jackson, R. G., 1977, Preliminary evaluation of lithofacies models for meandering alluvial streams, in A. D. Miall, ed., Fluvial sedimentology: Canadian Society of Petroleum Geologists Memoir 5, p. 543 - 576.

Jeannette, D. C., J. A. Bellian, C. Kerans, and J. R. Andrews, 2003, A breakthrough on the outcrop: new tools and techniques to bring outcrop studies into a 3-d workstation environment: Texas Bureau of Economic Geology Midyear Report 2003, p. 1 - 8.

Johnson, R. C., 1989, Geologic history and hydrocarbon potential of Late Cretaceous-age, low-permeability reservoirs, Piceance Basin, western Colorado: United States Geological Survey Bulletin 1787-E, 51 p.

Johnson, R. C. and T. M. Finn, 1986, Cretaceous through Holocene history of the Douglas Creek Arch, Colorado and Utah, in, D. S. Stone and K. S. Johnson, eds., New interpretations of northwest Colorado geology: Rocky Mountain Association of Geologists, p. 77 - 95.

Johnson, R. C. and D. D. Rice, 1990, Occurrence and geochemistry of natural gases, Piceance Basin, northwest Colorado: AAPG Bulletin, v. 74, no. 6, p. 805 - 829.

Jones, A., J. Doyle, T. Jacobsen, and D. Kjonsvik, 1995, Which sub-seismic heterogeneities influence waterflood performance? A case study of a low net-to-gross fluvial reservoir, in H. J. deHaan, ed., New developments in improved oil recovery: Geological Society Special Publication, no. 84, p. 5 - 18.

Joseph, P. et al., 2000, The Annot sandstone outcrop (French Alps): architecture description as input for quantification and 3-d reservoir modeling: Gulf Coast Section SEPM Foundation 20th Annual Research Conference, Deep Water Reservoirs of the World, Dec. 3 - 6, 2000.

Koltermann, C. E. and S. M. Gorelick, 1996, Heterogeneity in sedimentary deposits: a review of structure-imitating, process-imitating, and descriptive approaches: Water Resources Research, v. 32, no. 9, p. 2617 - 2658.

Kuuskraa, V. A., T. Barrett, R. Mueller, and J. Hansen, 1997, Reservoir characterization for development of Mesaverde Group sandstones of the Piceance Basin, Colorado, in E. B. Coalson, J. C. Osmond, and E. T. Williams, eds., Innovative applications of petroleum technology guidebook: Rocky Mountain Association of Geologists, p. 61 - 72.

Law, B. E., 2002, Basin-centered gas systems: AAPG Bulletin, v. 86, no. 11, p. 1891 - 1919.

Law, B. E. and C. W. Spencer, 1989, Geology of tight gas reservoirs in the Pinedale anticline area, Wyoming, and at the Multiwell Experiment site, Colorado: United States Geological Survey Bulletin 1886, p. A1 - A7.

Leeder, M. R., 1973, Fluviatile fining-upward cycles and the magnitude of paleochannels: Geological Magazine, v. 3, p. 265 - 276.

Leeder, M. R., 1978, A quantitative stratigraphic model for alluvium, with special reference to channel deposit density and interconnectedness, in A. D. Miall, ed., Fluvial sedimentology: Canadian Society of Petroleum Geologists Memoir 5, p. 587 - 596.

Leeder, M. R., 1999, Sedimentology and sedimentary basins, from turbulence to tectonics: Oxford, Blackwell Science Publishing, 592 p.

Leopold, L. B. and M. G. Wolman, 1960, River meanders: Geological Society of America Bulletin, v. 71, p. 769 - 794.

Li, H. and C. D. White, 2003, Geostatistical models for shales in distributary channel point bars (Ferron Sandstone, Utah): from ground-penetrating radar data to three-dimensional flow modeling: AAPG Bulletin, v. 87, no. 12, p. 1851 - 1868.

Lorenz, J. C., D. M. Heinz, J. A. Clark, and C. A. Searls, 1985, Determination of widths of meander-belt sandstone reservoirs from vertical downhole data, Mesaverde Group, Piceance Creek Basin, Colorado: AAPG Bulletin, v. 69, no. 5, p. 710 - 721.

Lorenz, J. C., 1989, Reservoir sedimentology of rocks of the Mesaverde Group, Multiwell Experiment site and east-central Piceance Basin, northwest Colorado, in B. E. Law and C. W. Spencer, eds., Geology of tight gas reservoirs in the Pinedale anticline area, Wyoming, and at the Multiwell

Experiment site, Colorado: United States Geological Survey Bulletin 1886, p. K1 - K24.

MacDonald, A. C. and E. K. Halland, 1993, Sedimentology and shale modeling of a sandstone-rich fluvial reservoir: Upper Statfjord Formation, Statfjord Field, northern North Sea: AAPG Bulletin, v. 77, no. 6, p. 1016 - 1040.

MacDonald, A. C., L. M. Falt, and A. L. Hektoen, 1998, Stochastic modeling of incised valley geometries: AAPG Bulletin, v. 82, no. 6, p. 1156 - 1172.

Mackey, S. D. and J. S. Bridge, 1995, Three-dimensional model of alluvial stratigraphy: theory and application: Journal of Sedimentary Research, v. B65, no. 1, p. 7 - 31.

Meandering River, 2004, <http://www.xpda.com/alaska02/>, Accessed April 14, 2004.

Miall, A. D., 1985, Architectural element analysis: a new method of facies analysis applied to fluvial deposits: Earth-Science Reviews, v. 22, p. 261 - 308.

Miall, A. D., 1988, Reservoir heterogeneities in fluvial sandstones: lessons from outcrop studies: AAPG Bulletin, v. 72, no. 6, p. 682 - 697.

Miall, A. D., 1996, The geology of fluvial deposits: Heidelberg, Springer-Verlag, 582 p.

Middleton, G. V., ed., 1965, Primary sedimentary structures and their hydrodynamic interpretation: SEPM Special Publication no. 12, 265 p.

Middleton, G. V., and J. B. Southard, 1978, Mechanics of sediment movement: SEPM Short Course no. 3, 244 p.

Miller, M. C., I. N. McCave, and P. D. Komar, 1977, Threshold of sediment motion under unidirectional currents: Sedimentology, v. 24, p. 507 - 527.

Nanson, G. C., 1980, Point bar and floodplain formation of the meandering Beatton River, northeastern British Columbia, Canada: Sedimentology, v. 27, p. 3 - 29.

Nelson, P. H. and J. E. Kibler, 2003, A catalog of porosity and permeability from core plugs in siliciclastic rocks: United States Geological Survey Open File Report 03-420, 6 p. plus attachments.

Nichols, G., 1999, Sedimentology & stratigraphy: Oxford, Blackwell Science Ltd, 355 p.

Novakovic, D., C. D. White, R. M. Corbeanu, W. S. Hammon, J. P. Bhattacharya, and G. A. McMechan, 2002, Hydraulic effects of shales in fluvial-deltaic deposits: ground-penetrating radar, outcrop observations, geostatistics, and three-dimensional flow modeling for the Ferron Sandstone, Utah: Mathematical Geology, v. 34, no. 7, p. 857 - 893.

Patterson, P. E., T. A. Jones, C. J. Donofrio, A. D. Donovan, and J. D. Ottmann, 2002, Geologic modeling of external and internal reservoir architecture of fluvial depositional systems, in M. Armstrong, C. Bettini, N. Champigny, and A. Galli, eds., Geostatistics Rio 2000, Proceedings of the Geostatistics Sessions of the 31st International Geological Congress, Rio de Janeiro, Brazil: Kluwer Academic Publishers, p. 41 - 52.

Patterson, P. E., K. Kronmueller, and T. D. Davies, 2003, Sequence stratigraphy of the Mesaverde Group and Ohio Creek Conglomerate, northern Piceance Basin, Colorado, in K. M. Peterson, T. M. Olsen, and D. S. Anderson, eds., Piceance Basin 2003 guidebook: Rocky Mountain Association of Geologists, p.115 - 129.

Payne, D. F., K. Tuncay, A. Park, J. B. Comer, and P. Ortoleva, 2000, A reaction-transport-mechanical approach to modeling the interrelationships among gas generation, overpressuring, and fracturing: implications for the Upper Cretaceous natural gas reservoirs of the Piceance Basin, Colorado: AAPG Bulletin, v. 84, p. 545 - 565.

Perry, W. J., M. A. Grout, R. L. Tang, and T. J. Hainsworth, 1988, Wedge model for late Laramide basement-involved thrusting, Grand Hogback monocline and White River uplift, western Colorado (abs.): Geological Society of America Abstracts with Programs, v. 20, no. 7, p. 384 - 385.

Plint, A. G., 1983, Sandy fluvial point-bar sediments from the Middle Eocene of Dorset, England, in J. D. Collinson and J. Lewin, eds., Modern and ancient fluvial systems: Special Publication of the International Association of Sedimentologists, no. 6, p. 355 - 368.

Pollack, D. W., 1988, Semi-analytical computation of path lines for finite-difference models: Ground Water, no. 6, p. 743 - 750.

Potential Gas Committee, 2003, Potential supply of natural gas in the United States: Report of the Potential Gas Committee (Dec. 31, 2002): Potential Gas Agency, Colorado School of Mines, Golden, CO, April 2003, 316 p. with accompanying cd-rom.

Puigdefabregas, C., 1973, Miocene point-bar deposits in the Ebro Basin, Northern Spain: Sedimentology, v. 20, p. 133 - 144.

Quigley, D. M., 1965, Geologic history of Piceance Creek-Eagle Basins: AAPG Bulletin v. 49, no. 11, p. 1974 - 1996.

Richards, P. C., 1992, An introduction to the Brent Group: a literature review, in A. C. Morton, R. S. Haszeldine, M. R. Giles, and S. Brown, eds., Geology of the Brent Group: Geological Society Special Publication no. 61, p. 15 - 26.

River Systems of the World, 2004, <http://www.rev.net/~aloe/river/> Accessed March 27, 2004.

Roxar, 2003a, RMSgeomod user guide: release 7.2, 168 p.

Roxar, 2003b, RMSgeoplex user guide: release 7.2, 274 p.

Schumm, S. A., 1963, A tentative classification of alluvial river channels: United States Geological Survey Circ. 477, 10 p.

Schumm, S. A., 1968, River adjustment to altered hydrologic regimen – Murrumbidgee River and paleochannels, Australia: United States Geological Survey Prof. Paper 598, 65 p.

Schumm, S. A., 1972, Fluvial paleochannels, in J. K. Rigby and W. K. Hamblin, eds., Recognition of ancient sedimentary environments: SEPM Special Publication 16, p. 98 - 107.

Sharp, J. M., S. Mingjuan, and W. E. Galloway, 2003, Heterogeneity of fluvial systems; control on density-driven flow and transport: Environmental and Engineering Geosciences, v. 9, no. 1, p. 5 - 17.

Simons, D. E. and E. V. Richardson, 1961, Forms of bed roughness in alluvial channels: Proceedings of the American Society of Civil Engineers, v. 87, part 1, p. 87 - 105.

Spencer, C. W., 1989, Review of characteristics of low-permeability gas reservoirs in Western United States: AAPG Bulletin, v. 73, p. 613 - 629.

Sprague, A., et al., 2003, Physical stratigraphy of clastic strata; a hierarchical approach to the analysis of genetically related stratigraphic elements for improved reservoir prediction (abs.): AAPG Bulletin, v. 87, n. 10, p. 1695 - 1696.

Stephen, K. D., J. D. Clark, and A. D. Gardiner, 2001, Outcrop-based stochastic modeling of turbidite amalgamation and its effects on hydrocarbon recovery: Petroleum Geoscience, v. 7, p. 163 - 172.

Stephen, K. D. and M. Dalrymple, 2003, Reservoir simulations developed from an outcrop of incised valley fill strata: AAPG Bulletin, v. 86, no. 5, p. 797 - 822.

Stiles, J. H. and J. M. Hutfilz, 1992, The use of routine and special core analysis in characterizing Brent Group reservoirs, U.K. North Sea: Journal of Petroleum Technology, v. 44, no. 6, p. 704 - 713.

Sullivan, M., G. Jensen, F. Goulding, D. Jennette, L. Foreman, D. Stern, 2000, Architectural analysis of deep-water outcrops: implications for exploration and development of the Diana sub-basin, western Gulf of Mexico: Gulf Coast Section SEPM Foundation 20th Annual Research Conference, Deep Water Reservoirs of the World, Dec. 3 - 6, 2000.

Swanson, D. C., 1993, The importance of fluvial processes and related reservoir deposits: Journal of Petroleum Technology, v. 45, p. 368 - 377.

Tanner, W. F., 1960, Helicoidal flow, a possible cause of meandering: Journal of Geophysical Research, v. 65, no. 3, p. 993 - 995.

Tweto, O., 1975, Laramide (the Cretaceous - early Tertiary) orogeny in southern Rocky Mountain, in Curtis B.F., ed., Cenozoic history of the southern Rocky Mountains: Geological Society of America Memoir 144, p. 1 - 44.

Tyler, K., A. Henriquez, and T. Svanes, 1994, Modeling heterogeneities in fluvial domains: a review of the influence on production profiles, in J. M. Yarus and R. L. Chambers, eds., Stochastic modeling and geostatistics; principles, methods, and case studies: AAPG Computer Applications in Geology no. 3, p. 77 - 89.

Tyler, R. and R. McMurry, 1995, Genetic stratigraphy, coal occurrence, and regional cross section of the Williams Fork Formation, Mesaverde Group, Piceance Basin, Northwestern Colorado: Colorado Geological Survey Open File Report 95-2, 42 p.

United States Geological Survey, 1955, Cameo Quadrangle, Colorado, Mesa County: United States Geological Survey 7.5 minute topographic series, scale 1:24,000, 1 sheet.

United States Geological Survey, 2003, Assessment of undiscovered oil and gas resources of the Uinta-Piceance Province of Utah and Colorado, 2002: United States Geological Survey Fact Sheet FS-157-02, 2 p.

United States Geological Survey, 2004, Digital elevation model of the Cameo and Round Mountain, Colorado Quadrangles, 30 m and 10 m resolution, available from <http://data.geocomm.com/>

Weber, K. J., 1982, Influence of common sedimentary structures on fluid flow in reservoir models: Journal of Petroleum Technology, March 1982, p. 665 - 672.

Willis, B. J., 1989, Palaeochannel reconstructions from point bar deposits: a three-dimensional perspective: Sedimentology, v. 36, p. 757 - 766.

Willis, B. J. and C. D. White, 2000, Quantitative outcrop data for flow simulation: Journal of Sedimentary Research, v. 70, no. 4, p. 788 - 802.

APPENDIX A

MEASURED SECTION DATA

Appendix A contains the descriptions of thirteen measured sections located on the three outcrops in Coal Canyon. Symbols used in the measured sections are explained in Appendix A.14. For measured section locations, refer to Appendix A.15 and Figures 2.1 and 2.2.

APPENDIX B

2-D OUTCROP MODELS

The attached compact disc entitled “Volume I” contains the RMS project files for all 2-D models generated in this study. These models were built using Roxar’s IRAP-RMS version 7.2. The following table describes the contents of each project file.

Project Filename	Description
2-D Lithology	Lithology modeling scenarios
2-D Grain Size	Grain-size model
2-D Petro Uniform	Porosity and permeability models with a uniform distribution
2-D Petro CST	Porosity and permeability models with a conditionally simulated distribution with an imposed trend
2-D Petro CS	Porosity and permeability models with a conditionally simulated distribution
2-D Petro GS	Porosity and permeability models with a distribution based on grain size
2-D Stream Uniform	Streamline simulations using uniformly distributed models
2-D Stream CST	Streamline simulations using conditionally simulated models with an imposed trend
2-D Stream CS	Streamline simulations using conditionally simulated models
2-D Stream GS	Streamline simulations using models based on grain-size distribution

APPENDIX C

LIDAR DATA

In the “Volume I” CD, under the folder “Lidar Data” is the original point-cloud data of the outcrop study area in Coal Canyon. There are seventeen images included and the data is formatted as x-y-z-intensity. These data can be viewed using Polyworks software. A decimated 3-D elevation model of the outcrop draped with intensity (VRML file) is included on the CD under the folder “Lidar Model”. Also in this folder is an IRAP-RMS project containing the Lidar surfaces, called “Coal Canyon Lidar”. Before viewing the VRML file, you must download Cosmo Player software, as described below:

1. Download Cosmo Player from the following website: http://www.ca.com/cosmo/ or use the .exe file included on the CD.

2. The included power point file entitled “Instructions for VRML” provides instructions and examples on how to use Cosmo Player.

3. The file “Coal Canyon Outcrops” is the VRML file of the three outcrops described in this study.

4. Now you can fly through the virtual outcrop. Notice the wild horse that was captured in the data at the base of the east outcrop!

APPENDIX D

2-D PETROPHYSICAL MODEL STATISTICS

APPENDIX E

ANALYSIS OF VARIANCE FOR 2-D MODELS

Appendix E.2. ANOVA results 2-D Lithology Models (not GS) Pore Volume

The results of an ANOVA statistical test performed at 14:27 on 20-MAY-2004

Source of Variation	Sum of Squares	d.f.	Mean Squares	F
between	24.39	2	12.20	0.4313
error	169.7	6	28.28	
total	194.1	8		

The probability of this result, assuming the null hypothesis, is 0.668

Group A: Number of items= 3
169. 170. 178.

Mean = 172.
95% confidence interval for Mean: 164.9 thru 179.9
Standard Deviation = 5.17
Hi = 178. Low = 169.
Median = 170.
Average Absolute Deviation from Median = 3.07

Group B: Number of items= 3
165. 166. 174.

Mean = 168.
95% confidence interval for Mean: 160.9 thru 175.9
Standard Deviation = 5.21
Hi = 174. Low = 165.
Median = 166.
Average Absolute Deviation from Median = 3.21

Group C: Number of items= 3
166. 168. 176.

Mean = 170.
95% confidence interval for Mean: 162.5 thru 177.5
Standard Deviation = 5.57
Hi = 176. Low = 166.
Median = 168.
Average Absolute Deviation from Median = 3.52

Appendix E.3. ANOVA results 2-D Lithology Models Pore Volume

The results of a ANOVA statistical test performed at 14:28 on 20-MAY-2004

Source of Variation	Sum of Squares	d.f.	Mean Squares	F
between	18.30	2	9.148	5.0957E-02
error	1616.	9	179.5	
total	1634.	11		

The probability of this result, assuming the null hypothesis, is 0.951

Group A: Number of items= 4
145. 169. 170. 178.

Mean = 166.
95% confidence interval for Mean: 150.4 thru 180.7
Standard Deviation = 14.4
Hi = 178. Low = 145.
Median = 169.
Average Absolute Deviation from Median = 8.49

Group B: Number of items= 4
145. 165. 166. 174.

Mean = 163.
95% confidence interval for Mean: 147.4 thru 177.7
Standard Deviation = 12.5
Hi = 174. Low = 145.
Median = 165.
Average Absolute Deviation from Median = 7.69

Group C: Number of items= 4
145. 166. 168. 176.

Mean = 164.
95% confidence interval for Mean: 148.6 thru 178.9
Standard Deviation = 13.3
Hi = 176. Low = 145.
Median = 167.
Average Absolute Deviation from Median = 8.38

Appendix E.4. ANOVA results 2-D Petrophysical Distributions Pore Volume

The results of a ANOVA statistical test performed at 14:30 on 20-MAY-2004

Source of Variation	Sum of Squares	d.f.	Mean Squares	F
between	1609.	3	536.3	170.5
error	25.16	8	3.145	
total	1634.	11		

The probability of this result, assuming the null hypothesis, is 0.000

Group A: Number of items= 3
166. 168. 170.

Mean = 168.
95% confidence interval for Mean: 165.5 thru 170.3
Standard Deviation = 1.81
Hi = 170. Low = 166.
Median = 168.
Average Absolute Deviation from Median = 1.21

Group B: Number of items= 3
165. 166. 169.

Mean = 167.
95% confidence interval for Mean: 164.2 thru 168.9
Standard Deviation = 2.30
Hi = 169. Low = 165.
Median = 166.
Average Absolute Deviation from Median = 1.47

Group C: Number of items= 3
174. 176. 178.

Mean = 176.
95% confidence interval for Mean: 174.0 thru 178.7
Standard Deviation = 2.00
Hi = 178. Low = 174.
Median = 176.
Average Absolute Deviation from Median = 1.33

Group D: Number of items= 3
145. 145. 145.

Mean = 145.
95% confidence interval for Mean: 142.6 thru 147.3

Standard Deviation = 0.000E+00
Hi = 145. Low = 145.
Median = 145.
Average Absolute Deviation from Median = 0.000E+00

Appendix E.5. ANOVA results 2-D Lithology Models (not GS) BTT

The results of a ANOVA statistical test performed at 14:16 on 20-MAY-2004

Source of Variation	Sum of Squares	d.f.	Mean Squares	F
between	1162.	2	580.8	24.43
error	142.7	6	23.78	
total	1304.	8		

The probability of this result, assuming the null hypothesis, is 0.001

Group A: Number of items= 3
28.0 29.0 32.0

Mean = 29.7
95% confidence interval for Mean: 22.78 thru 36.56
Standard Deviation = 2.08
Hi = 32.0 Low = 28.0
Median = 29.0
Average Absolute Deviation from Median = 1.33

Group B: Number of items= 3
40.0 52.0 55.0

Mean = 49.0
95% confidence interval for Mean: 42.11 thru 55.89
Standard Deviation = 7.94
Hi = 55.0 Low = 40.0
Median = 52.0
Average Absolute Deviation from Median = 5.00

Group C: Number of items= 3
20.0 22.0 24.0

Mean = 22.0
95% confidence interval for Mean: 15.11 thru 28.89
Standard Deviation = 2.00
Hi = 24.0 Low = 20.0
Median = 22.0
Average Absolute Deviation from Median = 1.33

Appendix E.6. ANOVA results 2-D Lithology Models BTT

The results of a ANOVA statistical test performed at 14:17 on 20-MAY-2004

Source of Variation	Sum of Squares	d.f.	Mean Squares	F
between	930.2	2	465.1	3.299
error	1269.	9	141.0	
total	2199.	11		

The probability of this result, assuming the null hypothesis, is 0.084

Group A: Number of items= 4
14.0 28.0 29.0 32.0

Mean = 25.8
95% confidence interval for Mean: 12.32 thru 39.18
Standard Deviation = 8.02
Hi = 32.0 Low = 14.0
Median = 28.5
Average Absolute Deviation from Median = 4.75

Group B: Number of items= 4
15.0 40.0 52.0 55.0

Mean = 40.5
95% confidence interval for Mean: 27.07 thru 53.93
Standard Deviation = 18.2
Hi = 55.0 Low = 15.0
Median = 46.0
Average Absolute Deviation from Median = 13.0

Group C: Number of items= 4
12.0 20.0 22.0 24.0

Mean = 19.5
95% confidence interval for Mean: 6.071 thru 32.93
Standard Deviation = 5.26
Hi = 24.0 Low = 12.0
Median = 21.0
Average Absolute Deviation from Median = 3.50

Appendix E.7. ANOVA results 2-D Distribution Scenarios BTT

The results of a ANOVA statistical test performed at 14:19 on 20-MAY-2004

Source of Variation	Sum of Squares	d.f.	Mean Squares	F
between	980.9	3	327.0	2.148
error	1218.	8	152.3	
total	2199.	11		

The probability of this result, assuming the null hypothesis, is 0.172

Group A: Number of items= 3
24.0 32.0 55.0

Mean = 37.0
95% confidence interval for Mean: 20.57 thru 53.43
Standard Deviation = 16.1
Hi = 55.0 Low = 24.0
Median = 32.0
Average Absolute Deviation from Median = 10.3

Group B: Number of items= 3
22.0 29.0 52.0

Mean = 34.3
95% confidence interval for Mean: 17.91 thru 50.76
Standard Deviation = 15.7
Hi = 52.0 Low = 22.0
Median = 29.0
Average Absolute Deviation from Median = 10.0

Group C: Number of items= 3
20.0 28.0 40.0

Mean = 29.3
95% confidence interval for Mean: 12.91 thru 45.76
Standard Deviation = 10.1
Hi = 40.0 Low = 20.0
Median = 28.0
Average Absolute Deviation from Median = 6.67

Group D: Number of items= 3
12.0 14.0 15.0

Mean = 13.7
95% confidence interval for Mean: -2.761 thru 30.09
Standard Deviation = 1.53
Hi = 15.0 Low = 12.0
Median = 14.0
Average Absolute Deviation from Median = 1.00

Appendix E.8. ANOVA results 2-D Lithology Models (not GS) Volume Swept

The results of a ANOVA statistical test performed at 14:22 on 20-MAY-2004

Source of Variation	Sum of Squares	d.f.	Mean Squares	F
between	3377.	2	1688.	98.51
error	102.8	6	17.14	
total	3480.	8		

The probability of this result, assuming the null hypothesis, is 0.000

Group A: Number of items= 3
145. 147. 154.

Mean = 148.
95% confidence interval for Mean: 142.7 thru 154.3
Standard Deviation = 4.44
Hi = 154. Low = 145.
Median = 147.
Average Absolute Deviation from Median = 2.83

Group B: Number of items= 3
128. 130. 137.

Mean = 132.
95% confidence interval for Mean: 125.8 thru 137.5
Standard Deviation = 4.73
Hi = 137. Low = 128.
Median = 130.
Average Absolute Deviation from Median = 3.00

Group C: Number of items= 3
99.0 101. 105.

Mean = 102.
95% confidence interval for Mean: 95.82 thru 107.5
Standard Deviation = 3.06
Hi = 105. Low = 99.0
Median = 101.
Average Absolute Deviation from Median = 2.00

Appendix E.9. ANOVA results 2-D Lithology Models Volume Swept

The results of a ANOVA statistical test performed at 14:24 on 20-MAY-2004

Source of Variation	Sum of Squares	d.f.	Mean Squares	F
between	2753.	2	1376.	1.588
error	7802.	9	866.9	
total	1.0554E+04	11		

The probability of this result, assuming the null hypothesis, is 0.257

Group A: Number of items= 4
72.0 145. 147. 154.

Mean = 129.
95% confidence interval for Mean: 96.07 thru 162.7
Standard Deviation = 38.4
Hi = 154. Low = 72.0
Median = 146.
Average Absolute Deviation from Median = 20.9

Group B: Number of items= 4
75.0 128. 130. 137.

Mean = 118.
95% confidence interval for Mean: 84.20 thru 150.8
Standard Deviation = 28.6
Hi = 137. Low = 75.0
Median = 129.
Average Absolute Deviation from Median = 16.0

Group C: Number of items= 4
67.0 99.0 101. 105.

Mean = 93.0
95% confidence interval for Mean: 59.70 thru 126.3
Standard Deviation = 17.5
Hi = 105. Low = 67.0
Median = 100.
Average Absolute Deviation from Median = 10.0

Appendix E.10. ANOVA results 2-D Petrophysical Distribution Volume Swept

The results of a ANOVA statistical test performed at 14:25 on 20-MAY-2004

Source of Variation	Sum of Squares	d.f.	Mean Squares	F
between	7068.	3	2356.	5.407
error	3486.	8	435.7	
total	1.0554E+04	11		

The probability of this result, assuming the null hypothesis, is 0.025

Group A: Number of items= 3
105. 130. 154.

Mean = 130.
95% confidence interval for Mean: 101.7 thru 157.3
Standard Deviation = 24.3
Hi = 154. Low = 105.
Median = 130.
Average Absolute Deviation from Median = 16.2

Group B: Number of items= 3
99.0 137. 145.

Mean = 127.
95% confidence interval for Mean: 99.21 thru 154.8
Standard Deviation = 24.6
Hi = 145. Low = 99.0
Median = 137.
Average Absolute Deviation from Median = 15.3

Group C: Number of items= 3
101. 128. 147.

Mean = 125.
95% confidence interval for Mean: 97.54 thru 153.1
Standard Deviation = 23.1
Hi = 147. Low = 101.
Median = 128.
Average Absolute Deviation from Median = 15.3

Group D: Number of items= 3
67.0 72.0 75.0

Mean = 71.3
95% confidence interval for Mean: 43.54 thru 99.12
Standard Deviation = 4.04
Hi = 75.0 Low = 67.0
Median = 72.0
Average Absolute Deviation from Median = 2.67

APPENDIX F

3-D POINT-BAR MODELS

The attached compact disc entitled “Volume II” contains the RMS project files for all 3-D models generated in this study. These models were built using Roxar’s IRAP-RMS version 7.2. The following table describes the contents of each project file.

Project Filename	Description
3-D Lithology	Lithology modeling scenarios
3-D Grain Size	Grain-size model
3-D Petro Uniform	Porosity and permeability models with a uniform distribution
3-D Petro CS	Porosity and permeability models with a conditionally simulated distribution
3-D Petro GS	Porosity and permeability models with a distribution based on grain size
3-D Volumetrics	Drainable volume and pore volume calculations
3-D Stream Uniform	Streamline simulations using uniformly distributed models
3-D Stream CS	Streamline simulations using conditionally simulated models
3-D Stream GS	Streamline simulations using models based on grain-size distribution

APPENDIX G

3-D PETROPHYSICAL MODEL STATISTICS

APPENDIX H

ANALYSIS OF VARIANCE FOR 3-D MODELS

Appendix H.1. ANOVA results 3-D Lithology Model Pore Volume

The results of a ANOVA statistical test performed at 15:13 on 20-MAY-2004

Source of Variation	Sum of Squares	d.f.	Mean Squares	F
between	2.4166E+05	2	1.2083E+05	1.3640E-03
error	5.3151E+08	6	8.8584E+07	
total	5.3175E+08	8		

The probability of this result, assuming the null hypothesis, is 0.999

Group A: Number of items= 3
7.838E+04 9.483E+04 9.512E+04

Mean = 8.944E+04
95% confidence interval for Mean: 7.6143E+04 thru 1.0274E+05
Standard Deviation = 9.580E+03
Hi = 9.512E+04 Low = 7.838E+04
Median = 9.483E+04
Average Absolute Deviation from Median = 5.578E+03

Group B: Number of items= 3
7.838E+04 9.423E+04 9.451E+04

Mean = 8.904E+04
95% confidence interval for Mean: 7.5742E+04 thru 1.0234E+05
Standard Deviation = 9.233E+03
Hi = 9.451E+04 Low = 7.838E+04
Median = 9.423E+04
Average Absolute Deviation from Median = 5.375E+03

Group C: Number of items= 3
7.838E+04 9.456E+04 9.483E+04

Mean = 8.926E+04
95% confidence interval for Mean: 7.5958E+04 thru 1.0255E+05
Standard Deviation = 9.420E+03
Hi = 9.483E+04 Low = 7.838E+04
Median = 9.456E+04
Average Absolute Deviation from Median = 5.483E+03

Appendix H.2. ANOVA results 3-D Petrophysical Distribution Pore Volume

The results of a ANOVA statistical test performed at 15:14 on 20-MAY-2004

Source of Variation	Sum of Squares	d.f.	Mean Squares	F
between	5.3139E+08	2	2.6569E+08	4397.
error	3.6259E+05	6	6.0431E+04	
total	5.3175E+08	8		

The probability of this result, assuming the null hypothesis, is 0.000

Group A: Number of items= 3
9.451E+04 9.483E+04 9.512E+04

Mean = 9.482E+04
95% confidence interval for Mean: 9.4469E+04 thru 9.5164E+04
Standard Deviation = 305.
Hi = 9.512E+04 Low = 9.451E+04
Median = 9.483E+04
Average Absolute Deviation from Median = 203.

Group B: Number of items= 3
9.423E+04 9.456E+04 9.483E+04

Mean = 9.454E+04
95% confidence interval for Mean: 9.4193E+04 thru 9.4888E+04
Standard Deviation = 297.
Hi = 9.483E+04 Low = 9.423E+04
Median = 9.456E+04
Average Absolute Deviation from Median = 198.

Group C: Number of items= 3
7.838E+04 7.838E+04 7.838E+04

Mean = 7.838E+04
95% confidence interval for Mean: 7.8033E+04 thru 7.8727E+04
Standard Deviation = 0.000E+00
Hi = 7.838E+04 Low = 7.838E+04
Median = 7.838E+04
Average Absolute Deviation from Median = 0.000E+00

Appendix H.3. ANOVA results 3-D Lithology Models BTT Well Pattern 1

The results of a ANOVA statistical test performed at 14:47 on 20-MAY-2004

Source of Variation	Sum of Squares	d.f.	Mean Squares	F
between	1.6324E+06	2	8.1618E+05	7.8846E-02
error	6.2109E+07	6	1.0352E+07	
total	6.3742E+07	8		

The probability of this result, assuming the null hypothesis, is 0.925

Group A: Number of items= 3
6.165E+03 1.139E+04 1.268E+04

Mean = 1.008E+04
95% confidence interval for Mean: 5535. thru 1.4627E+04
Standard Deviation = 3.452E+03
Hi = 1.268E+04 Low = 6.165E+03
Median = 1.139E+04
Average Absolute Deviation from Median = 2.173E+03

Group B: Number of items= 3
5.750E+03 1.010E+04 1.131E+04

Mean = 9.055E+03
95% confidence interval for Mean: 4509. thru 1.3601E+04
Standard Deviation = 2.925E+03
Hi = 1.131E+04 Low = 5.750E+03
Median = 1.010E+04
Average Absolute Deviation from Median = 1.853E+03

Group C: Number of items= 3
6.055E+03 1.090E+04 1.224E+04

Mean = 9.731E+03
95% confidence interval for Mean: 5186. thru 1.4277E+04
Standard Deviation = 3.253E+03
Hi = 1.224E+04 Low = 6.055E+03
Median = 1.090E+04
Average Absolute Deviation from Median = 2.061E+03

Appendix H.4. ANOVA results 3-D Petrophysical Distributions BTT Well Pattern 1

The results of a ANOVA statistical test performed at 14:48 on 20-MAY-2004

Source of Variation	Sum of Squares	d.f.	Mean Squares	F
between	6.1821E+07	2	3.0910E+07	96.54
error	1.9211E+06	6	3.2018E+05	
total	6.3742E+07	8		

The probability of this result, assuming the null hypothesis, is 0.000

Group A: Number of items= 3
1.131E+04 1.224E+04 1.268E+04

Mean = 1.208E+04
95% confidence interval for Mean: 1.1278E+04 thru 1.2876E+04
Standard Deviation = 701.
Hi = 1.268E+04 Low = 1.131E+04
Median = 1.224E+04
Average Absolute Deviation from Median = 458.

Group B: Number of items= 3
1.010E+04 1.090E+04 1.139E+04

Mean = 1.080E+04
95% confidence interval for Mean: 1.0001E+04 thru 1.1600E+04
Standard Deviation = 650.
Hi = 1.139E+04 Low = 1.010E+04
Median = 1.090E+04
Average Absolute Deviation from Median = 430.

Group C: Number of items= 3
5.750E+03 6.055E+03 6.165E+03

Mean = 5.990E+03
95% confidence interval for Mean: 5191. thru 6789.
Standard Deviation = 215.
Hi = 6.165E+03 Low = 5.750E+03
Median = 6.055E+03
Average Absolute Deviation from Median = 138

Appendix H.5. ANOVA results 3-D Lithology Models BTT Well Pattern 2

The results of a ANOVA statistical test performed at 14:50 on 20-MAY-2004

Source of Variation	Sum of Squares	d.f.	Mean Squares	F
between	5.9130E+06	2	2.9565E+06	8.454
error	2.0983E+06	6	3.4972E+05	
total	8.0113E+06	8		

The probability of this result, assuming the null hypothesis, is 0.018

Group A: Number of items= 3
1.610E+03 2.059E+03 2.519E+03

Mean = 2.063E+03
95% confidence interval for Mean: 1227. thru 2898.
Standard Deviation = 455.
Hi = 2.519E+03 Low = 1.610E+03
Median = 2.059E+03
Average Absolute Deviation from Median = 303.

Group B: Number of items= 3
2.763E+03 3.955E+03 4.340E+03

Mean = 3.686E+03
95% confidence interval for Mean: 2850. thru 4522.
Standard Deviation = 822.
Hi = 4.340E+03 Low = 2.763E+03
Median = 3.955E+03
Average Absolute Deviation from Median = 526.

Group C: Number of items= 3
1.490E+03 1.858E+03 2.305E+03

Mean = 1.884E+03
95% confidence interval for Mean: 1049. thru 2720.
Standard Deviation = 408.
Hi = 2.305E+03 Low = 1.490E+03
Median = 1.858E+03
Average Absolute Deviation from Median = 272.

Appendix H.6. ANOVA results 3-D Petrophysical Distribution BTT Well Pattern 2

The results of a ANOVA statistical test performed at 14:52 on 20-MAY-2004

Source of Variation	Sum of Squares	d.f.	Mean Squares	F
between	1.8447E+06	2	9.2233E+05	0.8974
error	6.1667E+06	6	1.0278E+06	
total	8.0113E+06	8		

The probability of this result, assuming the null hypothesis, is 0.456

Group A: Number of items= 3
2.305E+03 2.519E+03 4.340E+03

Mean = 3.055E+03
95% confidence interval for Mean: 1622. thru 4487.
Standard Deviation = 1.118E+03
Hi = 4.340E+03 Low = 2.305E+03
Median = 2.519E+03
Average Absolute Deviation from Median = 678.

Group B: Number of items= 3
1.858E+03 2.059E+03 3.955E+03

Mean = 2.624E+03
95% confidence interval for Mean: 1192. thru 4056.
Standard Deviation = 1.157E+03
Hi = 3.955E+03 Low = 1.858E+03
Median = 2.059E+03
Average Absolute Deviation from Median = 699.

Group C: Number of items= 3
1.490E+03 1.610E+03 2.763E+03

Mean = 1.954E+03
95% confidence interval for Mean: 522.0 thru 3387.
Standard Deviation = 703.
Hi = 2.763E+03 Low = 1.490E+03
Median = 1.610E+03
Average Absolute Deviation from Median = 424.

Appendix H.7. ANOVA results 3-D Lithology Models Volume Swept Well Pattern 1

The results of a ANOVA statistical test performed at 14:57 on 20-MAY-2004

Source of Variation	Sum of Squares	d.f.	Mean Squares	F
between	7.6965E+07	2	3.8483E+07	9.5930E-02
error	2.4069E+09	6	4.0115E+08	
total	2.4839E+09	8		

The probability of this result, assuming the null hypothesis, is 0.910

Group A: Number of items= 3
4.102E+04 7.742E+04 7.854E+04

Mean = 6.566E+04
95% confidence interval for Mean: 3.7362E+04 thru 9.3957E+04
Standard Deviation = 2.135E+04
Hi = 7.854E+04 Low = 4.102E+04
Median = 7.742E+04
Average Absolute Deviation from Median = 1.251E+04

Group B: Number of items= 3
3.822E+04 6.867E+04 7.058E+04

Mean = 5.916E+04
95% confidence interval for Mean: 3.0860E+04 thru 8.7455E+04
Standard Deviation = 1.816E+04
Hi = 7.058E+04 Low = 3.822E+04
Median = 6.867E+04
Average Absolute Deviation from Median = 1.079E+04

Group C: Number of items= 3
4.140E+04 7.668E+04 7.695E+04

Mean = 6.501E+04
95% confidence interval for Mean: 3.6714E+04 thru 9.3309E+04
Standard Deviation = 2.045E+04
Hi = 7.695E+04 Low = 4.140E+04
Median = 7.668E+04
Average Absolute Deviation from Median = 1.185E+04

Appendix H.8. ANOVA results 3-D Petrophysical Distributions Volume Swept Well Pattern 1

The results of a ANOVA statistical test performed at 14:59 on 20-MAY-2004

Source of Variation	Sum of Squares	d.f.	Mean Squares	F
between	2.3953E+09	2	1.1977E+09	81.13
error	8.8574E+07	6	1.4762E+07	
total	2.4839E+09	8		

The probability of this result, assuming the null hypothesis, is 0.000

Group A: Number of items= 3
7.058E+04 7.695E+04 7.854E+04

Mean = 7.536E+04
95% confidence interval for Mean: 6.9930E+04 thru 8.0787E+04
Standard Deviation = 4.213E+03
Hi = 7.854E+04 Low = 7.058E+04
Median = 7.695E+04
Average Absolute Deviation from Median = 2.654E+03

Group B: Number of items= 3
6.867E+04 7.668E+04 7.742E+04

Mean = 7.426E+04
95% confidence interval for Mean: 6.8829E+04 thru 7.9685E+04
Standard Deviation = 4.849E+03
Hi = 7.742E+04 Low = 6.867E+04
Median = 7.668E+04
Average Absolute Deviation from Median = 2.915E+03

Group C: Number of items= 3
3.822E+04 4.102E+04 4.140E+04

Mean = 4.021E+04
95% confidence interval for Mean: 3.4785E+04 thru 4.5642E+04
Standard Deviation = 1.739E+03
Hi = 4.140E+04 Low = 3.822E+04
Median = 4.102E+04
Average Absolute Deviation from Median = 1.062E+03

Appendix H.9. ANOVA results 3-D Lithology Models Volume Swept Well Pattern 2

The results of a ANOVA statistical test performed at 15:01 on 20-MAY-2004

Source of Variation	Sum of Squares	d.f.	Mean Squares	F
between	2.4846E+08	2	1.2423E+08	9.487
error	7.8566E+07	6	1.3094E+07	
total	3.2702E+08	8		

The probability of this result, assuming the null hypothesis, is 0.014

Group A: Number of items= 3
1.092E+04 1.442E+04 1.607E+04

Mean = 1.380E+04
95% confidence interval for Mean: 8688. thru 1.8914E+04
Standard Deviation = 2.632E+03
Hi = 1.607E+04 Low = 1.092E+04
Median = 1.442E+04
Average Absolute Deviation from Median = 1.719E+03

Group B: Number of items= 3
1.840E+04 2.713E+04 2.749E+04

Mean = 2.434E+04
95% confidence interval for Mean: 1.9227E+04 thru 2.9452E+04
Standard Deviation = 5.147E+03
Hi = 2.749E+04 Low = 1.840E+04
Median = 2.713E+04
Average Absolute Deviation from Median = 3.030E+03

Group C: Number of items= 3
1.006E+04 1.311E+04 1.485E+04

Mean = 1.267E+04
95% confidence interval for Mean: 7560. thru 1.7785E+04
Standard Deviation = 2.421E+03
Hi = 1.485E+04 Low = 1.006E+04
Median = 1.311E+04
Average Absolute Deviation from Median = 1.594E+03

Appendix H.10. ANOVA results 3-D Petrophysical Distribution Volume Swept Well Pattern 2

The results of a ANOVA statistical test performed at 15:02 on 20-MAY-2004

Source of Variation	Sum of Squares	d.f.	Mean Squares	F
between	6.7719E+07	2	3.3860E+07	0.7835
error	2.5930E+08	6	4.3217E+07	
total	3.2702E+08	8		

The probability of this result, assuming the null hypothesis, is 0.499

Group A: Number of items= 3
1.485E+04 1.607E+04 2.749E+04

Mean = 1.947E+04
95% confidence interval for Mean: 1.0181E+04 thru 2.8757E+04
Standard Deviation = 6.973E+03
Hi = 2.749E+04 Low = 1.485E+04
Median = 1.607E+04
Average Absolute Deviation from Median = 4.214E+03

Group B: Number of items= 3
1.311E+04 1.442E+04 2.713E+04

Mean = 1.822E+04
95% confidence interval for Mean: 8930. thru 2.7506E+04
Standard Deviation = 7.746E+03
Hi = 2.713E+04 Low = 1.311E+04
Median = 1.442E+04
Average Absolute Deviation from Median = 4.674E+03

Group C: Number of items= 3
1.006E+04 1.092E+04 1.840E+04

Mean = 1.313E+04
95% confidence interval for Mean: 3838. thru 2.2414E+04
Standard Deviation = 4.587E+03
Hi = 1.840E+04 Low = 1.006E+04
Median = 1.092E+04
Average Absolute Deviation from Median = 2.779E+03